THE FLORIDA STATE UNIVERSITY

COLLEGE OF ARTS AND SCIENCES

THE INFLUENCE OF COASTLINE GEOMETRY AND BOTTOM TOPOGRAPHY

ON THE EASTERN OCEAN CIRCULATION

By
HARLEY E. HURLBURT

A dissertation submitted to
the Department of Meteorology
in partial fulfillment of the
requirements for the degree of
Doctor of Philosophy

Approved:

Professor directing Dissertation

Richard A Cuiy

Perm Wright

T. N. Krishwemursi

March, 1974

ABSTRACT

An x-y-t two-layer, primitive equation model on a
β-plane has been developed to study the effects of longshore
variability on the wind-driven eastern ocean circulation.
Of particular interest are the effects of various configura-
tions of bottom topography and coastline geometry on the
wind-driven baroclinic coastal jet. The model is time-
dependent and retains the free surface. It is integrated
using an efficient semi-implicit numerical scheme and a
variable resolution grid which allows both resolution of
mesoscale boundary layers and longshore features, and a
model region with an E-W extent great enough to permit
development of a Sverdrup interior. A unique feature of
the model is an open-basin northern and southern boundary
condition which allows the development of a Sverdrup in-
terior even when the model is solved on regions with meso-
scale N-S extent.

The topographic β effect is found to play a funda-
mental role in the dynamics associated with mesoscale
longshore variations in topography. Due to the combination
of the wind stress and sloping topography, potential vortic-
ity is not well conserved. The streamlines show only a
slight tendency to parallel the isobaths. Longshore varia-
ity is not well conserved. The streamlines show only a
slight tendency to parallel the isobaths. Longshore varia-
tions in topography also produce barotropic flows required

for mass continuity extending far beyond the topographic feature. These flows appear to respond on a scale governed by the barotropic radius of deformation. Quite striking is the lack of large amplitude wave phenomena associated with mesoscale longshore topographic perturbations.

For mesoscale variations in coastline geometry the coastal currents and the pattern of vertical motion follow the coastline, but not with uniform strength. Thus, it is possible for strong upwelling to occur when not predicted by the local wind stress. It is also found that variations in coastline geometry may excite large amplitude internal Kelvin waves.

ACKNOWLEDGMENTS

The author especially wishes to acknowledge his
grateful appreciation to Dr. James J. O'Brien, his major
professor and thesis advisor, for stimulating his interest
in the coastal upwelling problem, involving him as a partner
in research in the early stages of his graduate career, and
for teaching him the fundamentals of numerical methods. In
addition, the author wishes to thank him for suggesting the
canyon case discussed in Section 4 and for his helpful com-
ments and suggestions on the manuscript and other aspects
of the present research. Appreciation is extended to Drs.
T. N. Krishnamurti, R. A. Craig, P. Wright, and Y. Hsueh
for serving as members of my doctoral committee. Thanks

for serving as members of my doctoral committee. Thanks
are due Mr. John Kindle and Dr. George Weatherly for reading
the manuscript and offering numerous helpful comments and

TABLE OF CONTENTS

LIST OF TABLES

LIST OF ILLUSTRATIONS

1. INTRODUCTION

An important feature of the eastern ocean circulation
is coastal upwelling. Associated with the upwelling is an
equatorward surface jet and a poleward undercurrent (Mooers
et al., 1972). The present investigation focuses attention
on the effects longshore variations in bottom topography
and coastline geometry have on these phenomena. To date the
effects of these longshore variations have received little
attention. Hence, we begin with a brief review of the dynam-
ics of the eastern ocean circulation as revealed by theo-
retical studies based on longshore-independent topography
and coastline geometry.

The first important contribution to the theory of
coastal upwelling was Ekman (1905). He considered a balance
between vertical friction, $\partial \vec{\tau}/\partial z$, and the Coriolis force in
the surface layer of a wind-driven ocean. For an equator-
ward wind stress in the eastern ocean such a balance predicts
offshore flow in a thin surface layer and one-sided divergence
at the coast. Mass continuity implies the occurrence of
coastal upwelling and a deep onshore flow (Thorade, 1909).
A convenient aspect of this simple theory is the uncoupling
of the vertically-integrated horizontal momentum equations.
A convenient aspect of this simple theory is the uncoupling
of the vertically-integrated horizontal momentum equations.
As a result it is possible to understand the gross features

1

of the circulation in a vertical cross-section normal to the coast without considering the longshore flow at all.

Subsequently, many investigators have studied the theory of the wind-driven eastern ocean circulation. Ekman dynamics has been an important element of most of the theories. We will consider only a few which are particularly relevant to the present study.

Hidaka (1954) and Yoshida (1955) attempted to understand the coastal circulation in the vertical plane normal to the coast. Hidaka's homogeneous, **steady** state model predicts upwelling confined to a viscous boundary layer of thickness $(A/f)^{1/2}$, where A is the horizontal eddy viscosity and f is the Coriolis parameter. Using a time-dependent model which includes stratification, Yoshida found a characteristic width scale for coastal upwelling given by the baroclinic radius of deformation. This is a more realistic result in the light of observations (Mooers et al., 1972). Yoshida also argued that for an equatorward wind stress parallel to the coast both an equatorward surface jet and poleward undercurrent should exist, but presented no clearly defined theory.

Charney (1955) made an important contribution to the theory of the eastern ocean circulation when he applied conservation of potential vorticity to a theory of wind-driven coastal jets. However, Charney intended his theory for application to the Gulf Stream, and its relevance to

the eastern ocean circulation was overlooked until O'Brien
and Hurlburt (1972) found a coastal jet with similar
dynamics in their numerical model.

The time-dependent model of O'Brien and Hurlburt
(1972) consists of two layers of finite depth, is on an
f-plane and neglects all longshore derivatives. Later
O'Brien (1973) solved a linear, inviscid version of this
model with a flat bottom analytically. He found that the
longshore flow consists of a barotropic mode governed by
the barotropic radius of deformation, and a baroclinic mode
governed by the baroclinic radius of deformation, both of
which grow linearly with time under steady wind stress
forcing parallel to the coast. Although the modes are
oppositely directed, they have the same amplitude at the
coast which precludes development of the observed under-
current.

Allen (1973) also found the surface jet in a continu-
ously stratified f-plane model which neglects all longshore
derivatives, but because he used the rigid lid approximation,
his model does not contain a realistic treatment of the
barotropic mode. The rigid lid imposes an integral con-
straint which requires the net transport normal to the
coast to be zero at any point. This is a good approximation
for his f-plane model only if the width of the basin is much
coast to be zero at any point. This is a good approximation
for his f-plane model only if the width of the basin is much
less than the barotropic radius of deformation.

These f-plane models which neglect all longshore derivatives are missing a key dynamical ingredient, the longshore pressure gradient. Garvine (1971) investigated a homogeneous, steady-state model and demonstrated the longshore pressure gradient is an essential dynamical element of a homogeneous model of coastal upwelling. Without this longshore pressure gradient the subsurface onshore flow required by mass continuity must occur in a strong bottom Ekman layer in his model, a feature not in accord with observations (Mooers et al., 1972). Inclusion of this pressure gradient also yields oppositely directed longshore coastal currents in the surface and subsurface layers. However, their dynamics and associated horizontal and vertical structure suffer defects which are unavoidable when a homogeneous fluid is used to represent a stratified ocean. No physical mechanism for the production of a longshore pressure gradient of just the magnitude required to balance the onshore flow is included in Garvine's model, but he suggested that the "wind 'piles up' the water in the direction of the stress."

Yoshida (1967) found an equatorward surface current and poleward undercurrent in a wind-driven steady state model of the eastern ocean circulation on a β-plane. However, the occurrence of these currents in his model depends on a particular parameterization of thermohaline mixing and the existence of a Sverdrup balance within the upwelling zone. ticular parameterization of thermohaline mixing and the existence of a Sverdrup balance within the upwelling zone. Scale analysis is sufficient to show that such dynamics are not operant in the coastal upwelling circulation.

Hurlburt and Thompson (1973) investigated a time-dependent two-layer model on a vertical cross-section normal to a meridional coast which neglects longshore derivatives of the velocity field and the wind stress, but which retains the N-S pressure gradient and the β effect. For an equatorward wind stress and flat topography the longshore flow is characterized by a Sverdrup interior and geostrophically balanced jets in the upwelling boundary layer consisting of an equatorward surface jet and a poleward undercurrent. The offshore flow in the upper layer is Ekman drift reduced by the presence of the N-S sea surface slope. The compensating onshore flow in the lower layer is geostrophic.

From the point of view of vorticity dynamics the jet structure predicted by the model is most succinctly explained as a Sverdrup interior matched to an upwelling boundary layer in which potential vorticity is conserved. For the simple case of flat topography and no wind stress curl in the upwelling zone Hurlburt and Thompson were able to obtain a stronger result even for a dynamically much more general case. They demonstrated the vertically integrated longshore mass transport must nearly vanish point by point across the upwelling boundary layer.

Consideration of the momentum balance also led them to expect the development of an equatorward surface jet and a poleward undercurrent. In the upper layer the offshore to expect the development of an equatorward surface jet and a poleward undercurrent. In the upper layer the offshore flow outside the upwelling zone is Ekman drift reduced by

the N-S pressure gradient force. The onshore flow in the
lower layer is geostrophically balanced outside the upwelling
zone. Inside the upwelling zone this combination of geo-
strophy and Ekman drift breaks down to satisfy the kinematic
boundary condition. Thus, in this region there is equator-
ward acceleration in the upper layer and poleward in the
lower layer.

The momentum and vorticity dynamics can be linked by
noting that under the assumptions of the model the Sverdrup
flow is independent of latitude, but the E-W pressure gradi-
ent required for this flow to be geostrophically balanced is
not. Hence, the Hurlburt and Thompson model develops a N-S
sea surface slope which is independent of latitude for a N-S
independent wind stress. Note that the appropriate N-S pres-
sure gradient develops in response to the vorticity constraint
of a Sverdrup interior and is not specified, and also that a
N-S pressure gradient will develop in this manner only in
basins large enough, $0(10^3$ by 10^3 km), to admit a Sverdrup
interior.

In the present study an x-y-t two-layer, primitive
equation model on a β-plane is used to investigate three-di-
mensional aspects of the wind-driven eastern ocean circula-
tion. The model is time dependent and retains the free
surface. It is integrated using an efficient semi-implicit

surface. It is integrated using an efficient semi-implicit
numerical scheme and a variable resolution grid which allows
resolution of mesoscale boundary layers and longshore features,

and a model region with an E-W extent great enough to permit development of a Sverdrup interior. A unique feature of the model is an open-basin northern and southern boundary condition which allows development of a Sverdrup interior even when the model is solved on regions with mesoscale N-S extent. Such a model is useful in studying the effects on the eastern ocean circulation of northern and southern boundary conditions, and longshore variations in the wind stress, bottom topography, and coastline geometry. Details of the model formulation are discussed in Section 2, and some tests of the boundary conditions in Section 3.

To date observational and theoretical studies of the three-dimensional eastern ocean circulation have been very limited. The effects of a closed basin have been studied by Pedlosky (1974), using a steady state model on an f-plane driven by an arbitrary wind stress distribution. He has also studied the effects of a closed basin, positive wind stress curl in the eastern ocean, and a continental slope as three factors affecting the direction and strength of currents in the eastern boundary layers (Pedlosky, personal communication).

Gill and Clarke (1973) and Suginohara (1973) have studied the effects of longshore variations in an equator-ward wind stress both with and without longshore independent shelf-slope topography. They found that Kelvin wave and ward wind stress both with and without longshore independent shelf-slope topography. They found that Kelvin wave and continental shelf wave dynamics are important in understanding their results. In particular, Suginohara **found** that

when the wind is turned off the subsiding upwelled portion

of the pycnocline propagates poleward at the speed of an

internal Kelvin wave. He also found a poleward undercurrent

in the flat bottom case, but reported that none develops

until the wind is shut off in a case with a longshore inde-

pendent continental shelf slope similar to that off Oregon.

It should be noted that Suginohara's solutions are essential-

ly for a closed basin with a rigid lid on an f-plane, since

his basin (about 300 by 1500 km) is not large enough to

develop a Sverdrup interior. The N-S pressure gradient and

poleward undercurrent in his model are primarily the result

of the solid northern and southern boundaries and the exist-

ence of the wind stress. That is, the mass continuity con-

straint imposed by the closed basin and the distribution of

the wind reduces the amplitude of the barotropic mode for

the N-S flow from that which would occur in the absence of

N-S derivatives. Some additional effects of the wind stress

distribution are discussed in Section 3_c.

Attention in this study is focussed on the effects of

various configurations of bottom topography (Section 4) and

coastline geometry (Section 5) on the eastern ocean circula-

tion. Several theoretical studies have considered the

effects of topography without longshore variations (e.g.,

Hurlburt and Thompson, 1973). These studies show that for

an equatorward wind stress parallel to the coast, enhanced

Hurlburt and Thompson, 1973). These studies show that for

an equatorward wind stress parallel to the coast, enhanced

upwelling should occur near the shelf break. However, the

only other study known to the author which includes topo-
graphic longshore variations is the diagnostic model cur-
rently under investigation by Peng and Hsueh (personal
communication).

In the present study the topographic β effect is
found to play a fundamental role in the dynamics associated
with mesoscale, 0(100 km), longshore variations in topo-
graphy by affecting the strength of the longshore flow.
Thus, this influence and mass continuity require currents
normal to the coast which appear to respond on a scale
governed by the barotropic radius of deformation. Due to
the combination of the wind stress and sloping topography,
potential vorticity is not well conserved. The streamlines
show only a slight tendency to follow the isobaths. Quite
striking is the lack of wave phenomena associated with the
mesoscale topographic perturbations.

Arthur (1965) and Yoshida (1967) have discussed the
effects of capes in terms of steady state flows, assuming
the strength of the basic current is unaffected by the
presence of the cape. Arthur writes the relative vorticity
in natural coordinates and bases his discussion on a scale
analysis of the vorticity equation. Yoshida considers capes
with amplitudes small compared to the width of the basic
longshore currents. Both conclude the strongest upwelling
should occur on the south side of capes.
longshore currents. Both conclude the strongest upwelling
should occur on the south side of capes.

In the present time dependent study the effects of
coastline variations with mesoscale, 0(100 km), amplitude

and length scales are investigated. The width of the coastal currents is less than the amplitude of the coastline features. It is found that coastal currents and the pattern of vertical motion follow the coastline, but not with uniform strength. Along some parts of the coastline the wind may be normal to the coast. Thus, it is possible for strong upwelling to occur when not predicted by the local wind stress. Preferred regions for upwelling are identified, but it is found that when the winds are cut off the whole pattern of vertical motion propagates poleward along the coast at the speed of an internal Kelvin wave. Hence, significant upwelling may occur along any part of coastline feature after the wind has been cut off. In general it is found that variations in coastline geometry may excite large amplitude internal Kelvin waves.

2. THE MODEL

a. Model equations

The model equations are the vertically-integrated primitive equations for a stably stratified, rotating ocean on a β-plane. The origin is at the coast and a reference level below the sea surface. The hydrostatic and Boussinesq approximations are used and the effects of atmospheric pressure gradients and tidal potential are ignored. Thermodynamics and thermohaline mixing are also neglected. Their omission is discussed in Section 3.

Under the assumptions given, the momentum equations and equations of continuity form the following closed set for an x-y-t two-layer model on a β-plane.

$$\frac{\partial \vec{V}_1}{\partial t} + \vec{V}_1 \cdot \nabla \vec{V}_1 + \hat{k} \times f\vec{V}_1 = - g\nabla (h_1 + h_2 + D) + \frac{\vec{\tau}_s - \vec{\tau}_I}{\rho h_1} +$$

$$+ A\nabla^2 \vec{V}_1 \qquad (1)$$

$$\frac{\partial h_1}{\partial t} + \nabla \cdot (h_1 \vec{V}_1) = 0 \qquad (2)$$

$$\frac{\partial \vec{V}_2}{\partial t} + \vec{V}_2 \cdot \nabla \vec{V}_2 + \hat{k} \times f\vec{V}_2 = - g\nabla (h_1 + h_2 + D) + g'\nabla h_1 +$$

$$+ \frac{\vec{\tau}_I - \vec{\tau}_B}{\rho h_2} + A\nabla^2 \vec{V}_2 \qquad (3)$$

$$\frac{\partial h_2}{\partial t} + \nabla \cdot (h_2 \vec{V}_2) = 0 \qquad (4)$$

$$\frac{\partial h_2}{\partial t} + \nabla \cdot (h_2 \vec{V}_2) = 0 \qquad (4)$$

11

where 1 denotes the upper layer, 2 the lower layer,

$$\nabla = \frac{\partial}{\partial x}\hat{i} + \frac{\partial}{\partial y}\hat{j}$$

$$\vec{V}_i = u_i\hat{i} + v_i\hat{j}$$

$$f = f_0 + \beta(y - y_0)$$

$$g' = g(\rho_2 - \rho_1)/\rho_2 \tag{5}$$

$$\vec{\tau}_s = \tau_{sx}\hat{i} + \tau_{sy}\hat{j}$$

$$\vec{\tau}_I = \rho C_I|\vec{V}_1 - \vec{V}_2|(\vec{V}_1 - \vec{V}_2)$$

$$\vec{\tau}_B = \rho C_B|\vec{V}_2|\vec{V}_2$$

and i = 1, 2. Symbols are defined in Appendix A, although most of the notation used is common in oceanography. D(x) represents the height of the bottom topography above a reference level. The formulation of the interfacial and bottom stresses follows O'Brien and Hurlburt (1972), but has been modified slightly to be invariant under coordinate transformation.

b. Boundary conditions

The eastern and western boundary conditions are kinematic and no slip. These conditions may also be used at the northern and southern boundaries to form a closed basin. However, to investigate mesoscale phenomena it may for economic reasons be highly advantageous to solve the model on limited portions of basins. Immediately two related problems

arise. The first is the formulation of appropriate boundary conditions. The second is the realistic representation of large scale features of the circulation, such as a Sverdrup interior, which may exert an important influence on the mesoscale circulation. These two problems have been overcome in the present investigation by using a boundary condition based on the x-z plane model of Hurlburt and Thompson (1973) which neglects longshore derivatives of the velocity field and the wind stress, but which retains the N-S pressure gradient and the β effect. This condition permits development of a Sverdrup interior even when the portion of the basin solved has only a mesoscale N-S extent. However, the E-W scale, O(1000 km) or more, cannot be relaxed if the model is to develop a Sverdrup interior without the imposition of some additional constraint.

The formulation of the boundary condition is discussed in Appendix B. Two crucial requirements for it to be applicable are that the longshore flow be nearly geostrophic and that

$$\left| \int_{-L_x}^{x} f \, \frac{\partial v_i}{\partial y} \, dx \right| << \left| \int_{-L_x}^{x} \beta v_i \, dx \right|$$

near the northern and southern boundaries, where $-L_x$ is at the western boundary and $i = 1, 2$. Since $f (\partial v_i/\partial y)$ may be comparable to βv_i in the eastern boundary layers, the latter comparable to βv_i in the eastern boundary layers, the latter requirement essentially demands that the N-S pressure gradient exhibit only a second order change across these eastern layers.

In short, the boundary condition, which we will refer to as quasi-symmetric because of its partial neglect of long-shore derivatives, sets $\partial/\partial y = 0$ in (1) through (4) except for the N-S pressure gradient in the momentum equations and $\partial h_i v_i/\partial y$ in the continuity equations. The N-S pressure gradients are given by

$$g \frac{\partial}{\partial y} (h_1 + h_2 + D) = \int_{-L_x}^{x} \beta (v_1 - v_A) \, dx +$$

$$+ g \frac{\partial}{\partial y} (h_1 + h_2 + D)\Big|_{-L_x} \tag{6}$$

$$g \frac{\partial}{\partial y} (h_1 + h_2 + D) - g' \frac{\partial h_1}{\partial y} = \int_{-L_x}^{x} \beta (v_2 + \frac{h_1}{h_2} v_A) \, dx +$$

$$+ g \frac{\partial}{\partial y} (h_1 + h_2 + D)\Big|_{-L_x} - g' \frac{\partial h_1}{\partial y}\Big|_{-L_x} \tag{7}$$

where

$$v_A = v_1 - \left[v_1 h_1 + \left(v_2 + \frac{g'}{f} \frac{\partial h_1}{\partial x} \right) h_2 \right] \bigg/ (h_1 + h_2) \tag{8}$$

Application of the Hurlburt and Thompson model as a boundary condition has required two modifications which are discussed in Appendix B. Some tests of the boundary condition are discussed in Section 3. These demonstrate that solutions for a closed basin on a β-plane, the quasi-symmetric boundary conditions described here, and the x-z plane model of Hurlburt and Thompson are essentially the same in the interior and the eastern ocean. They may be different in the western ocean, if the N-S pressure gradients at the western boundary of the quasi-symmetric condition are not determined by an ocean, if the N-S pressure gradients at the western boundary of the quasi-symmetric condition are not determined by an integral constraint on the total mass flux through the northern and southern boundaries.

Hurlburt and Thompson show that the N-S pressure gradient which develops due to the vorticity constraint of a Sverdrup interior responds primarily to the geostrophic N-S flow. Due to (8) the inertial oscillations and Ekman drift do not affect the N-S pressure gradient in the northern and southern boundary condition. Several other techniques for the removal of ageostrophic components from v in (6) and (7) have been investigated, but the use of (8) is the only one which has not led to instabilities such as amplification of the fundamental barotropic E-W mode of the basin.

c. Initial conditions

In most cases the model has been started from rest with no horizontal pressure gradients. However, the cases discussed in Section 5 have been integrated twice, once starting from rest, and a second time starting from the following quasi-balanced initial state with a Sverdrup interior:

$$u_1 = \frac{H_2}{H_1 + H_2} \left(\frac{\tau_{sy}}{\rho H_1 f} \right) (1 - e^{-r/\lambda}) \tag{9}$$

$$u_2 = - \frac{H_1}{H_2} u_1 \tag{10}$$

$$v_1 = v_2 = \frac{1}{\rho \beta (H_1 + H_2)} \operatorname{curl}_z \vec{\tau}_s \tag{11}$$

$$\tag{12}$$

$$H_1 = \text{constant}$$

$$\tag{12}$$

$$H_1 = \text{constant}$$

$$H_2 = (H_2 + D) \Big|_{-L_x} - D + \frac{f}{\beta \rho g (H_1 + H_2)} \left[\tau_{sy} - \tau_{sy} \Big|_{-L_x} \right] \tag{13}$$

where r is the distance from the boundary and λ is the baro-clinic radius of deformation,

$$\lambda = \frac{NH_1}{f} \qquad (14)$$

For the two-layer model the Brunt-Väisälä frequency, N, is given by

$$N^2 = \frac{g'H_2}{H_1(H_1 + H_2)} \qquad (15)$$

The flow normal to the coast is a combination of geostrophy and Ekman drift which obeys the constraint, (10), required by the Sverdrup interior. The internal mode for the flow normal to the coast is brought to zero on a scale determined by the baroclinic radius of deformation.

In all cases the wind stress has been applied impulsive-ly at initial time. This results in inertial oscillations, Rossby waves, and gravity waves which at times obscure aspects of the low frequency dynamics. Use of the quasi-balanced initial state reduces the amplitude of inertial oscillations, Rossby waves, and Kelvin waves and other gravity waves up to three orders of magnitude without significant alteration of the low frequency dynamics of the solutions. This has been verified by numerical experiment. In Section 5 solutions driven from rest are compared with solutions driven from the quasi-balanced initial state. It can be shown analytically that a gradual increase in the magnitude of the wind stress quasi-balanced initial state. It can be shown analytically that a gradual increase in the magnitude of the wind stress with a time constant of two days (a more expensive procedure) would reduce the amplitude of the inertial oscillations by only about one order of magnitude.

d.   Numerical formulation

The numerical model is specifically designed to exa-
mine boundary layer phenomena and to handle various configura-
tions of bottom topography and coastline geometry. However,
proper inclusion of β-plane dynamics, which Hurlburt and
Thompson (1973) have demonstrated exert a major influence on
the eastern ocean circulation, requires a minimum basin width
of about 1000 km, while proper resolution of the eastern
boundary layers requires $\Delta x < 5$ km, where Δx is the grid in-
crement in the E-W direction. The appropriate Δy is deter-
mined by the longshore scales of wind stress, bottom topography,
and coastline geometry. In the case of a closed basin the
need to resolve boundary layers along the northern and southern
walls may be an important consideration.

The number of grid points required is greatly reduced by
using a variable resolution grid in both x and y directions.
A different technique to vary the resolution is employed in
each direction. In the x-direction the variation of Δx is
discontinuous, and Δx is changed by factors ranging typically
from 1.5 to 4. This technique allows flexible distribution
of the fine mesh and large changes in Δx over a small number
of grid points. It also allows the same value of Δx along
all parts of a variable coastline. In most cases to be dis-
cussed Δx varies from about 3 to 300 km and changes several

cussed Δx varies from about 3 to 300 km and changes several
times across the basin. As an example, Δx versus x for a
case to be discussed in Section 5 is given in Table 1.

Table 1. Δx versus x

Mesh boundaries in km from eastern boundary	Δx in km
0	
120	4
150	6
180	10
300	30
600	100
4500	300
4800	100
4920	40
5000	20

The y-coordinate is stretched analytically by a change of independent variable. The stretched variable is defined by

$$s(a) \;=\; c\left[\alpha a + \sum_{k=1}^{N} \tanh\left(\frac{a - a_k}{\gamma_k}\right) + b\right], \tag{16}$$

a functional form used for this purpose by Schulman (1970). The constants b and c are chosen such that

$$s(0) \;=\; 0 \quad \text{and} \quad s(1) \;=\; 1 \tag{17}$$

Thus,

$$b \;=\; \sum_{k=1}^{N} \tanh\left(\frac{a_k}{\gamma_k}\right) \tag{18}$$

$$\text{\textit{c}} \;=\; \left[\sum_{k=1}^{N} \tanh\left(\frac{}{\gamma_k}\right) \quad \left(1 - a_k\right)\right]^{-1} \tag{19}$$

$$c \;=\; \left[\alpha + b + \sum_{k=1}^{N} \tanh\left(\frac{1 - a_k}{\gamma_k}\right)\right]^{-1} \tag{19}$$

Since

$$q = q(s(a(y))) \tag{20}$$

where q is any dependent variable and

$$a = y/L_y, \tag{21}$$

the first and second derivatives in y are given by

$$\frac{dq}{dy} = \frac{1}{L_y}\frac{ds}{da}\frac{dq}{ds} \tag{22}$$

$$\frac{d^2q}{dy^2} = \frac{1}{(L_y)^2}\left(\frac{ds}{da}\right)^2\frac{d^2q}{ds^2} + \frac{1}{(L_y)^2}\frac{d^2s}{da^2}\left(\frac{dq}{ds}\right)^2 \tag{23}$$

Hence, this technique is particularly simple to incorporate in existing code without a stretched variable. In all cases to be discussed $N = 1$ and $a_1 = 0.5$. The values of the stretching parameters, α and γ_1, vary from case to case. At most Δy varies by a factor of 12, from 5 to 60 km, for some cases discussed in Section 5.

The finite difference scheme is explicit in the y-direction and semi-implicit in the x-direction, so a time step greater than allowed by the usual CFL condition is possible. In the x-direction the terms responsible for the fastest propagating waves in the system, the internal and external gravity waves, are treated implicitly using a scheme patterned after Kwizak and Robert (1971), but which is sufficiently different that it is explained in detail by O'Brien and Hurlburt (1972). The diffusive terms are also treated im-different that it is explained in detail by O'Brien and Hurlburt (1972). The diffusive terms are also treated implicitly in the x-direction using the Crank-Nicholson (1947) scheme.

To determine the velocity components in each row
(x-direction), a pair of coupled tridiagonal matrices must
be inverted. The tridiagonal property, which allows effici-
ent inversion of the matrices, may be retained despite the
discrete changes in Δx by computing derivatives in terms of
the fine grid increment rather than the coarse at points
where Δx changes. At these points an interpolative differ-
encing technique is employed such that

$$\frac{\partial u}{\partial x} \simeq (u_{j+1} - [1 - \epsilon] u_j - \epsilon u_{j-1})/2\Delta x_2, \tag{24}$$

$$\frac{\partial^2 u}{\partial x^2} \simeq (u_{j+1} - [1 + \epsilon] u_j + \epsilon u_{j-1})/\Delta x_2^2 \tag{25}$$

and

$$\frac{\partial uv}{\partial x} \simeq \{(u_j + u_{j+1})(v_j + v_{j+1}) - ([2-\epsilon]u_j + \epsilon u_{j-1})([2-\epsilon]v_j$$
$$+ \epsilon v_{j-1})\}/4\Delta x_2 \tag{26}$$

where $\epsilon = \Delta x_2/\Delta x_1 < 1$, and j is the grid point index. Except
for a practical upper bound on ϵ^{-1} which varies from problem
to problem, there is no restriction on ϵ or the spacing of
points at which Δx is changed. The model has proved very ef-
ficient in terms of core storage and for min Δy >> min Δx
in terms of computing time. Thus, it has been feasible to
compute a number of cases, $O(100)$.

Other properties of the finite difference scheme
include leap-frog time differencing and Scheme F from Grammel-
tvedt (1969), which makes use of quadratic averaging, for the

advective terms. The frictional terms are lagged in time except for the implicit treatment of horizontal friction in the x-direction mentioned earlier. Since the order of the leap-frog time differencing scheme is greater than the order of the differential equations, the first time step is a forward difference. Differencing at the boundaries is one sided. In particular

$$\frac{\partial h_i u_i}{\partial x} \simeq -[h_i(0,y,t) + h_i(-\Delta x,y,t)]u_i(-\Delta x,y,t)/2\Delta x \quad (27)$$

is used over flat topography where $i = 1, 2$, and $u_i(0,y,t) = 0$. Over sloping topography

$$\frac{\partial h_i u_i}{\partial x} \simeq -h_i(-\Delta x,y,t)u_i(-\Delta x,y,t)/\Delta x \quad (28)$$

was found to yield superior results. A continuous check showed mass conservation $O(10^{-3}$ per cent) or better for the cases to be discussed.

e. Model parameters

We need only specify the model parameters to complete the formulation of the model. Parameter values given in Table 2 are those used in Section 5, and unless otherwise noted, are used in the other cases as well. The cases discussed in Section 5 are driven by the steady wind stress distribution shown in Fig. 1. Minor variations depending on the width of the basin are used in other cases. Unless

the width of the basin are used in other cases. Unless otherwise noted, the stress distribution is independent of the y-coordinate. In some cases the wind has been shut off
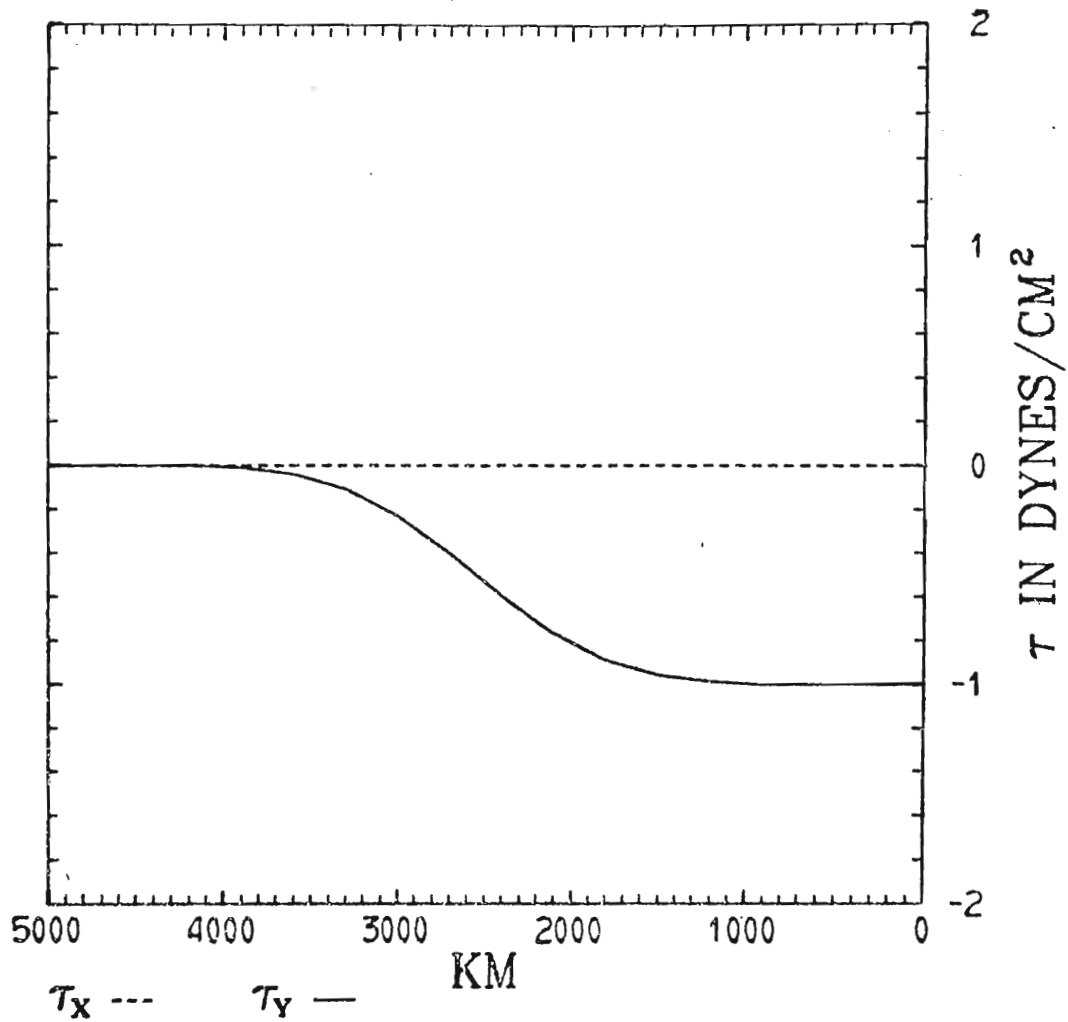
Fig. 1. E-W profiles of the wind stress components: τ_{sy} is -1 dyn cm^{-2} in the eastern ocean; τ_{sx} is zero every-where.

Table 2. Model parameters

Parameter	Value	Parameter	Value
A	10^6 cm^2 sec^{-1}	H_1	50 m
C_B	10^{-3}	H_2	150 m
C_I	10^{-5}	L_x	5000 km
f_0	4×10^{-5} sec^{-1}	L_y	800 to 1000 km
g	10^3 cm sec^{-2}	β	$2 \times 10^{-13} cm^{-1} sec^{-1}$
g'	2 cm sec^{-2}	ρ	1 gm cm^{-3}

at day 5 to examine the spin-down process. For the wind stress in Fig. 1 $curl_z \vec{\tau}_s$ ranges from 0 to -6.7×10^{-9} dyn cm^{-3}.

An interfacial stress coefficient of $C_I = 10^{-5}$ is used as suggested by Thompson and O'Brien (1973). A bottom stress coefficient of $C_B = 10^{-3}$ is prescribed after Proudman (1953). Hurlburt and Thompson (1973) have shown that the value of the N-S pressure gradient at the western boundary should have little effect on the eastern circulation of an ocean with a Sverdrup interior. Hence, in the northern and southern boundary conditions the N-S pressure gradients at the western boundaries are arbitrarily set to zero. The solution in the eastern ocean is also nearly independent of the wind stress distribution outside the eastern boundary solution in the eastern ocean is also nearly independent of the wind stress distribution outside the eastern boundary layers, provided a Sverdrup balance exists just west of these layers.

An attempt has been made to choose parameter values which are realistic for the eastern ocean. In particular the stratification and the layer thicknesses are based on observations in this region. For example, observations show that the upwelling circulation is confined to the upper few hundred meters (e.g., see Mooers et al., 1972). Fortunately, the qualitative results of the model solutions are quite insensitive to the less certain frictional parameters: A, C_B, and C_I, at least within the range of physically plausible values. However, the value of A is quantitatively significant, e.g., see the comparison of solutions using $A = 10^6$ and 10^7 cm^2 sec^{-1} by Hurlburt and Thompson (1973). The observational literature for the Oregon coastal region alone suggests a wide range of values for A. Stevenson et al. (1973) find values from about 10^4 to 10^7 cm^2 sec^{-1}. Mooers et al. (1972) calculate values from (2 to 5)$\times 10^5$ cm^2 sec^{-1} for low passed data with a half power point at 40 hr.

3. PRELIMINARY ANALYSIS OF THE MODEL

a. Review of basic model dynamics

The dynamics of the eastern ocean circulation on a β-plane for a long, straight meridional coast are discussed in detail by Hurlburt and Thompson (1973) and have been summarized in the introduction. Suffice it to note here that the longshore flow is nearly geostrophic. A Sverdrup balance is a characteristic feature of the interior solution for an ocean scale basin. For an interior solution which nearly eliminates the barotropic mode (e.g., a Sverdrup interior) the interior flow normal to the eastern boundary consists of Ekman drift reduced by the N-S pressure gradient in the upper layer, and is geostrophic in the lower layer. As explained in the introduction, the breakdown of this combination of geostrophy and Ekman drift in the eastern boundary layers leads to the development of coastal jets.

Fig. 2 shows a solution at day 5 for a flat bottom case driven from rest by a y-independent equatorward wind stress with an E-W distribution similar to that of Fig. 1. The half amplitude point is 1500 km from both eastern and western boundaries. The wind stress curl ranges from 0 to -10^{-8} dyn cm^{-3}. Δx ranges from 1 to 200 km, $\Delta y = 200$ km,
and $\Delta t = 30$ min. The other parameters are given in Table 2
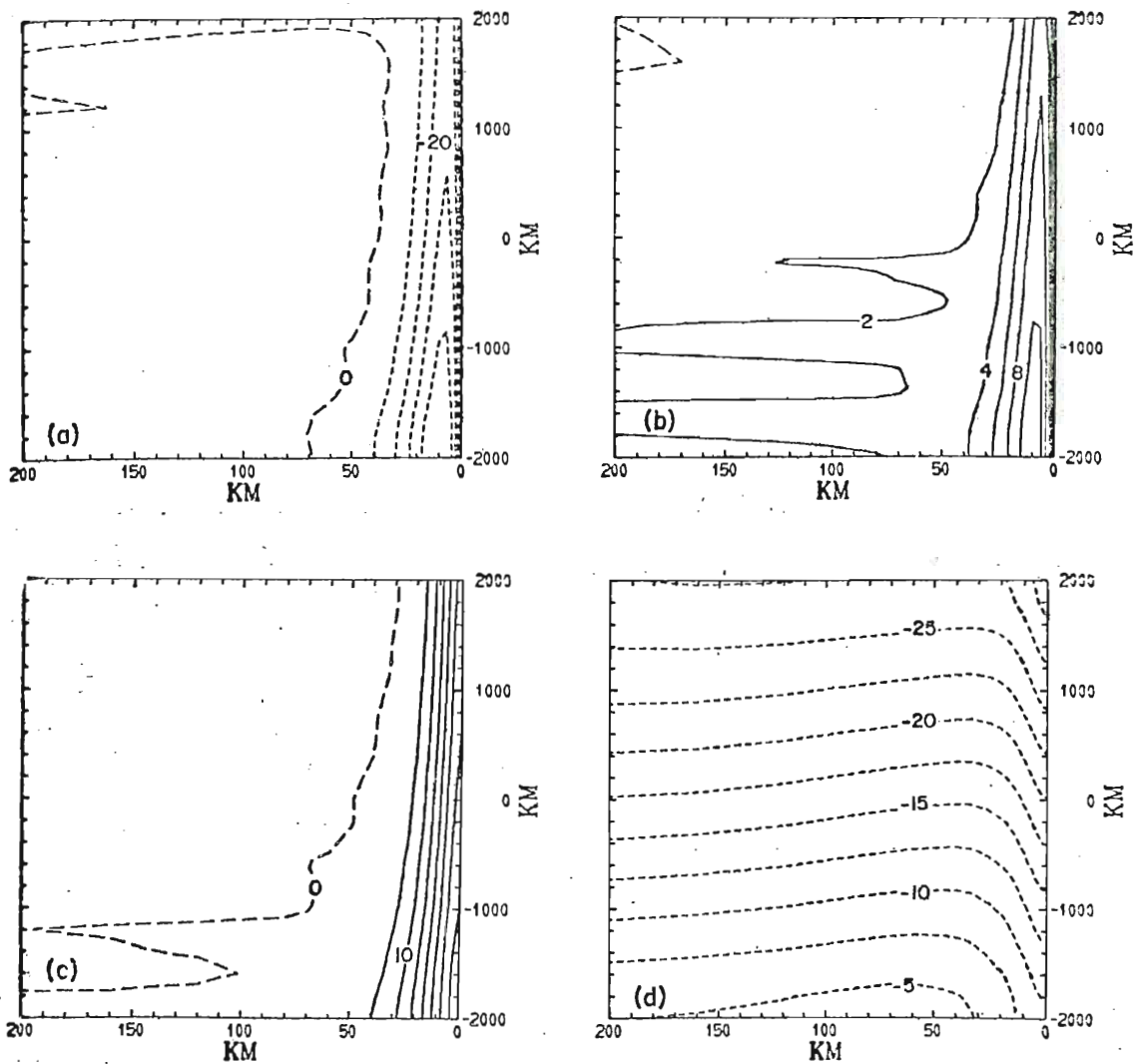
Fig. 2.   Solution at day 5 for a flat bottom case on a β-plane with a y-independent wind stress and quasi-symmetric northern and southern boundary conditions.   The model region is 3000×4000 km, but only the eastern 200 km of greatest interest are shown.   The N-S velocity components (cm sec^{-1}) show an equatorward surface jet (a), a poleward undercurrent (b), and weak interior flow.   The pycnocline height anomaly (c) in m shows upwelling near the eastern boundary.   The free surface anomaly (d) in cm shows the N-S pressure gradient and indicates the geo-poleward undercurrent (b), and weak interior flow.   The pycnocline height anomaly (c) in m shows upwelling near the eastern boundary.   The free surface anomaly (d) in cm shows the N-S pressure gradient and indicates the geo-strophic nature of the equatorward surface jet.

except that L_x = 3000 km and L_y = 4000 km. Fig. 2a,b shows the equatorward surface jet, poleward undercurrent, and weak interior flow. The N-S waves, which are especially prominent in Fig. 2b, decrease in wavelength with time, and occur because the inertial period is a function of latitude. Fig. 2c,d shows the pycnocline height anomaly and the free surface anomaly. The height anomaly is defined as the departure of a surface from its initial position. The width scale for the upwelling is governed approximately by the baroclinic radius of deformation,(14). The N-S pressure gradient and the eastern boundary layer are clearly evident in the free surface. Note that the coastal jets and the upwelling markedly decrease in amplitude with latitude, although linear inviscid theory (O'Brien, 1973) predicts their amplitude to be independent of latitude. The decrease with latitude occurs because the radius of deformation $\propto f^{-1}$, whereas the width of the viscous boundary layer is nearly independent of latitude, i.e., in the y-momentum equation the width of the viscous boundary layer is given by

$$L_v \simeq \left(\frac{Av}{fu}\right)^{1/2} \tag{29}$$

where $u \propto f^{-1}$. Since v/u = 0(10), the longshore flow may be nearly geostrophic even into the hydrostatic viscous boundary layer.

The following sub-sections discuss briefly some addi-
layer.

The following sub-sections discuss briefly some additional fundamental characteristics of the model in terms of

simple case studies. Topics include the neglect of thermo-
dynamics and thermohaline mixing, open basin versus closed
basin, f-plane versus β-plane, the western ocean solution,
and the effects of N-S sloping topography and coastline
orientation.

b. Neglect of thermodynamics
   and thermohaline mixing

As mentioned in Section 2, thermodynamics and thermo-
haline mixing have been neglected in the x-y-t two-layer
model under investigation. However, Thompson (1974) has in-
cluded them in a two-layer x-z plane model which incorpo-
rates β-plane dynamics in the same manner as Hurlburt and
Thompson (1973). His model demonstrates that the inclusion
of thermodynamics and thermohaline mixing becomes important
when the interface between the two layers exhibits large
departures from its initial position, but for small depar-
tures his solutions are in essential agreement with the
Hurlburt and Thompson model in which density is constant
within a given layer.

In the present model the interface between the
layers surfaces in slightly over 6 days at low latitudes
(approximately 15°) for the parameters in Table 2, when
driven from rest by the steady wind stress shown in Fig. 1.
Beyond day 5 most of the solutions discussed in Sections 3,
4, and 5 must be considered suspect at low latitudes except
Beyond day 5 most of the solutions discussed in Sections 3,
4, and 5 must be considered suspect at low latitudes except
in the cases where the wind has been shut off at day 5.

c. Open basin versus closed basin

Before we discuss the effects of coastline geometry and longshore variations in the bottom topography, it is necessary to assess the role of the northern and southern boundary conditions and β-plane dynamics in the model. The seven case studies listed below are quite helpful in determining these roles.

1. f-plane, closed basin, $f = 10^{-4} \sec^{-1}$.

2. β-plane, closed basin, $f = (4 \text{ to } 14) \times 10^{-5} \sec^{-1}$, $\beta = 2 \times 10^{-13} \text{ cm}^{-1} \sec^{-1}$.

3. Linear variation in β, closed basin, $f = (4 \text{ to } 12) \times 10^{-5} \sec^{-1}$, $\beta = (2.2 \text{ to } 1.6) \times 10^{-13} \text{ cm}^{-1} \sec^{-1}$.

4. β-plane, quasi-symmetric northern and southern boundary conditions, $f = (4 \text{ to } 14) \times 10^{-5} \sec^{-1}$, $\beta = 2 \times 10^{-13} \text{ cm}^{-1} \sec^{-1}$.

5. Same as 4, but with y-independent wind stress.

6. Quasi-symmetric x-z plane model of Hurlburt and Thompson (1973) which neglects longshore derivatives of the velocity field, but includes the N-S pressure gradient and the β effect (see also Introduction and Section 2b), $f = 10^{-4} \sec^{-1}$, $\beta = 2 \times 10^{-13} \text{ cm}^{-1} \sec^{-1}$.

7. x-z, f-plane model of O'Brien and Hurlburt (1972), $f = 10^{-4} \sec^{-1}$.

Some of the salient results are summarized in Table 3 at a latitude where $f = 10^{-4}$. In all cases the bottom topography is flat and $L_x = 3000$ km. In the x-y-t cases $L_y = 5000$ km

Table 3. Open basin versus closed basin at day 6

Case	v_1 at jet max (cm/sec)	v_2 at jet max or 8 km from coast (cm/sec)	$v_{barotropic}$ 50 km from coast (cm/sec)	Pycno- cline height anomaly at coast (m)	β (cm^{-1} sec^{-1}) $\times 10^{-13}$	y coord (km) $-2500 \leq y \leq 2500$
1	-39.4	2.7	-5.9	35.5	0	500
2	-34.9	7.5	.5	36.4	2	500
3	-34.8	7.0	-.5	36.0	1.8	900
4	-34.0	7.5	1.1	36.6	2	500
5	-33.8	8.9	2.1	36.4	2	500
6	-32.4	8.4	1.5	35.1	2	--
7	-51.2	-11.4	-19.8	35.2	0	--

and y_0 = -2500 km. The E-W distribution of the wind stress is the same as for the case discussed in Section 3a. In Cases 1, 2, and 3 the N-S distribution of τ_{sy} is y-independent between y = ±1500 km, but is gradually brought to zero near the northern and southern boundaries to avoid the necessity of resolving strong boundary layers near these boundaries. The N-S distribution of τ_{sy} for Case 4 is y-independent between y = ±1000 km, but is gradually brought to zero at y = ±2000 km. In all the cases Δt = 30 min, Δx = 2.5 to 200 km, and in the x-y-t cases Δy = 100 km. Other parameter values are those given in Table 2.

Note the results in Table 3 are essentially the same Other parameter values are those given in Table 2.

Note the results in Table 3 are essentially the same for the cases which retain planetary vorticity advection

(Cases 2 through 6), but the f-plane cases (1 and 7) differ from these substantially. These are the expected results, if the Sverdrup interior exerts an important influence on the eastern ocean circulation. The similarity of Cases 2 through 6 is necessary if the x-y-t two-layer model with quasi-symmetric northern and southern boundary conditions is to be a useful model of the eastern ocean circulation.

Several additional aspects of these solutions are worthy of note. First, it is clear that under the assumptions of the model $\partial v_i/\partial y = 0$ or at least

$$\left| \int_{-L_x}^{x} f \frac{\partial v_i}{\partial y} \, dx \right| << \left| \int_{-L_x}^{x} \beta v_i \, dx \right|$$

at initial time and after the establishment of a Sverdrup interior (cf. Section 2b). However, if this is not true during the adjustment process, it is conceivable that the effect of $f \, (\partial v_i/\partial y)$ on the N-S pressure gradient might systematically compensate for that of βv_i through Rossby waves with y variations. In that case the development of a Sverdrup interior might occur on a longer time scale than that predicted by the Hurlburt and Thompson (1973) model. This should not occur, since the excitation and properties of the Rossby waves are independent of latitude in the model (except for Case 3), although the geostrophic adjustment process is not. The similarity of Cases 2 in the model (except for Case 3), although the geostrophic adjustment process is not. The similarity of Cases 2 through 6 also demonstrates that the approximations made by Hurlburt and Thompson do not artificially reduce the

time scale for the development of a Sverdrup interior. In all the cases (except Case 7) a poleward undercurrent appears in less than one day.

Case 3 (linear variation in β) shows that physically realistic variations in β do not significantly alter the solutions, although the time scale for the development of the Sverdrup interior is slightly increased in the poleward portion of the basin where β is smaller. Substitution of the Sverdrup relation

$$v_1 h_1 + v_2 h_2 \; = \; \frac{1}{\rho\beta} \, \text{curl}_z \, \vec{\tau}_s \tag{30}$$

into (6) or (7) ($v_1 \simeq v_2$) demonstrates that, to within the approximations made in deriving the quasi-symmetric boundary condition, the N-S pressure gradient is independent of the value of β in a Sverdrup interior.

Only Cases 2, 3, and 4 begin to develop a western boundary current. Cases 5 and 6 would also develop a western boundary current if a non-zero N-S pressure gradient was specified at the western boundary of the quasi-symmetric condition. This would best be done by imposing an integral constraint on the total mass flux through the cross-section at which the quasi-symmetric condition is applied. However, the Sverdrup interior and consequently the eastern ocean circulation are essentially independent of the western ocean solution as verified by Cases 2 through 6. See Hurlburt and circulation are essentially independent of the western ocean solution as verified by Cases 2 through 6. See Hurlburt and Thompson (1973) for additional discussion of this topic.

In the β-plane case the barotropic mode may be nearly eliminated by the vorticity constraint expressed by the Sverdrup balance,(30). In the f-plane case this constraint no longer exists, but constraints due to mass continuity may still exert a controlling influence on the development of the barotropic mode.

To investigate this problem numerical experiments on an f-plane (not included in Table 3) were conducted using three different sets of boundary conditions at $y = \pm 2500$ km: closed basin, $\partial h_i/\partial y = 0$ in the momentum equations, and $\partial v_i/\partial y = 0$ in the continuity equations. Note application of the second and third boundary conditions simultaneously over specifies the problem. In all the experiments the wind stress is longshore and exhibits a y-dependence like Case 4 with $L_y = 5000$ km. Both x-dependent and x-independent distributions are used, and $L_x = 200$ km or 3000 km.

The experiments show that the magnitude of the N-S pressure gradient and consequently the magnitude of the barotropic mode for the f-plane case are affected by the distribution of the wind stress, the proximity of boundaries, and the type of boundary conditions used. In all the cases the barotropic mode is weaker than in Case 7, and in most cases at least a weak poleward undercurrent develops in the upwelling zone. The barotropic mode for a closed basin on ~~an f-plane is eliminated completely only if the depth and~~ upwelling zone. The barotropic mode for a closed basin on an f-plane is eliminated completely only if the depth and the wind stress are uniform across the basin in the direction

normal to the wind stress. This mode is also eliminated in a similar case with $\partial h_1/\partial y = 0$ at the boundaries, $y = \pm 2500$ km.

The following vertically integrated barotropic equations on an f-plane plus geostrophy in the longshore flow yield some additional insight into the f-plane dynamics, especially the manner in which the pattern of the wind stress may affect the N-S pressure gradient:

$$g\ \frac{\partial \zeta}{\partial y}\ =\ \int_{-L_x}^{x}\ f\ \frac{\partial v}{\partial y}\ dx\ +\ g\ \frac{\partial \zeta}{\partial y}\bigg|_{-L_x} \tag{31}$$

$$\frac{\partial v}{\partial t}\ =\ -\ g\ \frac{\partial \zeta}{\partial y}\ +\ \frac{\tau_{sy}}{\rho h}\ -\ fu \tag{32}$$

ζ is the free surface anomaly and h is the total depth. Eq. (31) is obtained by assuming geostrophy for the long-shore flow, integrating the vorticity equation in x and comparing the result with the y-momentum equation. Especially in the absence of a Sverdrup interior, $f\ \partial v/\partial y$ is not a small term in the vorticity equation in some regions. This may result in large variations of the N-S pressure gradient in the x-direction. For the f-plane cases these variations are accurately described by (31).

Note in (32) there are three competing mechanisms for the longshore acceleration. In the Sverdrup interior of a β-plane solution the Coriolis term nearly vanishes, ror tne longshore acceleration. In the Sverdrup interior of a β-plane solution the Coriolis term nearly vanishes, the N-S pressure gradient approximately balances the wind stress, and little or no barotropic mode develops. In

the f-plane case (32) suggests the initial development of
$v < 0$ in the region forced by $\tau_{sy} < 0$, but $v \simeq 0$ north and
south of this region. (Directional terminology is used for
convenience in this f-plane discussion by assuming the
same orientation as the β-plane cases.) Mass continuity
then demands $u > 0$ in the northern part of the forced region
and $u < 0$ in the southern part. Thus, (32) shows $\partial v/\partial y < 0$
in both the region forced by the wind stress and in the
region of compensating northward flow west of the forced
region. In the absence of a N-S pressure gradient at the
western boundary (31) shows this leads to $\partial h/\partial y < 0$, and
from (32) retardation in the development of the barotropic
mode. The N-S pressure gradient at the western boundary
develops in response to the demands of mass continuity
imposed by the boundary conditions.

Much more could be said about these solutions, but
our interest here is limited to the f-plane, β-plane com-
parison, noting that mechanisms exist in an f-plane model
which may reduce the barotropic mode. However, only in a
few special cases do they match or exceed the effectiveness
of a Sverdrup interior. For a given solution using an ocean
scale basin and a longshore wind stress, the relative im-
portance of the f-plane and β-plane mechanisms to the under-
current would depend primarily on the scale of the wind
portance of the f-plane and β-plane mechanisms to the under-
current would depend primarily on the scale of the wind
stress distribution and the direction of the coastline.
Yoshida (1973) also discusses the effect of the wind stress

distribution on the barotropic mode, and hence the prospects
for the development of a counter-undercurrent in the eastern
boundary layer.

The amplitude of the Rossby waves in the closed basin
is less than in the open basin because part of the N-S pres-
sure gradient required by a Sverdrup interior develops to
satisfy mass continuity on a slightly shorter time scale
associated with barotropic gravity waves. This accounts for
much of the slight differences in the barotropic mode and
the strength of the coastal jets between Case 2 and Cases 4,
5, and 6. These slight discrepancies should be reduced if
the N-S pressure gradients at the western boundary of the
quasi-symmetric condition are determined by an integral
constraint on the total mass flux through the cross-section
at which the quasi-symmetric condition is applied.

At this point it seems clear that the solutions using
quasi-symmetric northern and southern boundary conditions
with the N-S pressure gradients at the western boundary
arbitrarily set to zero provide satisfactory interior and
eastern ocean solutions for the simple case of flat topo-
graphy and no wind stress curl in the eastern ocean, at least
on the several day time scale of the integrations. This is
not surprising, because for a solution with an eastern bound-
ary layer which conserves potential vorticity matched to a
not surprising, because for a solution with an eastern bound-
ary layer which conserves potential vorticity matched to a
Sverdrup interior, all the dependent variables except in the
western ocean are determined by dynamical constraints which

are internal, linked to the wind stress forcing or to the
eastern boundary, but which are independent of the western,
northern and southern boundaries. This is also true for a
dynamically more general case with a flat bottom and no wind
stress curl in the upwelling zone as demonstrated by Hurlburt
and Thompson (1973). They show that the net longshore trans-
port must nearly vanish point by point where $\mathrm{curl}_z \ \vec{\tau}_s = 0$,
even inside the upwelling boundary layers.

The preceding theorems no longer hold in the upwelling
zone when there is sloping topography or wind stress curl in
the eastern ecean, or when a breakdown in the Sverdrup
interior occurs just outside the eastern boundary layers.
In such cases the northern and southern boundaries may play
a significant role in the determination of the barotropic
component of the longshore flow. This suggests the impor-
tance of determining the N-S pressure gradients at the
western boundaries of the quasi-symmetric boundary conditions
by an integral constraint on the total mass flux through the
boundary. This has not been done for any of the solutions
to be discussed and may be a deficiency in the solutions
discussed in Section 4. This should not be a serious defi-
ciency, since closed basin solutions on an f-plane with
sloping topography in the eastern ocean (but no closed con-
tours of topography) found by the author and by Suginohara
(1973) show little or no poleward undercurrent when driven
from rest by a steady equatorward wind stress. A similar

result is obtained in most of the solutions discussed in Section 4. Suginohara does report that an undercurrent develops when the wind is shut off. (Recall Suginohara has found essentially an f-plane solution because the size of his basin is only 250×1550 km, not wide enough to develop a Sverdrup interior.)

It should be noted that when u_2 is subgeostrophic, $\partial v_2/\partial t > 0$; when u_2 is supergeostrophic, $\partial v_2/\partial t < 0$ until a frictional balance develops. From (10) the onshore flow may become supergeostrophic in the presence of sloping topography, indicating that a bottom Ekman layer may be important in these regions. This suggests the possibility of a triple jet structure in the lower layer: a poleward undercurrent along the continental slope, equatorward flow closer to shore and possibly a narrow and weak poleward flow very near the coast as found by Hurlburt and Thompson (1973) in their sharp shelf case. A continuously stratified model could reveal this complicated structure better than a two layer model. As suggested by McNider and O'Brien (1973), it would be highly advantageous to allow the interfaces of layered models to intersect the sloping topography in order to reveal a poleward undercurrent along the continental slope.

Positive wind stress curl in the upwelling zone would enhance the poleward flow next to the coast as revealed in

enhance the poleward flow next to the coast as revealed in an experiment done by Hurlburt and Thompson (1973). Two experiments with positive wind stress curl in the upwelling

zone have been performed using the x-y-t two layer model in a closed basin on an f-plane. One experiment uses a flat bottom, the other y-independent sloping topography along the eastern boundary. In the flat bottom case the flow in the upwelling zone develops a strong, 0(10 cm/sec) barotropic poleward component. The case with sloping topography de- velops a narrower and weaker barotropic poleward component. These results can be understood by re-examination of the barotropic y-momentum equation, (32). The Coriolis term is weak near the coast in regions where the wind stress is y-independent, and as discussed earlier, the N-S pressure gradient exhibits only a second order change across the upwelling zone (whether f-plane or β-plane). Thus, positive wind stress curl in the eastern boundary regions favors poleward acceleration for the barotropic mode and negative wind stress curl and sloping topography favor equatorward acceleration. Note in a β-plane solution this wind stress curl itself would cause a second order change in the N-S pressure gradient across the eastern boundary layers.

d. Effect of N-S sloping
   topography

The effect of N-S sloping topography in conjunction with an equatorward wind stress has been investigated in one experiment. The topography is x-independent, flat in the southern 1000 km, exhibits a slope of 5×10^{-5} in the central experiment. The topography is x-independent, flat in the southern 1000 km, exhibits a slope of 5×10^{-5} in the central 2000 km, and is flat again in the northern 1000 km. The

model uses an open basin on an f-plane with $f = 4 \times 10^{-5}$ sec^{-1}, and is driven from rest by the y-independent wind stress used for the case in Section 3a. The value of β simulated by the topography is given by

$$\beta_T = \frac{f}{h} \frac{\partial h}{\partial y} , \tag{33}$$

where h is the total depth. Over the sloping portion of the basin, it ranges from 10^{-13} cm^{-1} sec^{-1} at the southern limit of the slope to 2×10^{-13} cm^{-1} sec^{-1} at the northern limit. L_x = 3000 km and L_y = 4000 km. Parameters not defined above are given in Table 2.

In six days of model time a well defined Sverdrup-like interior does not develop, but the barotropic mode is sufficiently reduced over the sloping topography that a poleward undercurrent with a maximum of 9 cm/sec develops in the upwelling zone by day 5. The poleward flow does not extend beyond the sloping region. Accounting for a difference in depth, a barotropic mode identical to that of Case 7 in Section 3c develops in the flat regions.

In this and in the preceding sub-section several different means for reducing or eliminating the barotropic mode with varying degrees of realism have been noted. This elimination could also be accomplished by using an open basin on an f-plane and specifying appropriate values for the N-S pressure gradients at the western boundaries of the quasi-symmetric boundary conditions. Also, the width of the basin required gradients at the western boundaries of the quasi-symmetric boundary conditions. Also, the width of the basin required could be reduced by using a large value of β. All the techniques mentioned which eliminate the barotropic mode in

the eastern ocean would yield similar solutions in the
upwelling zone. Those which allow the use of smaller basin
widths might reduce the computing cost. However, the use
of artificial devices to eliminate the barotropic mode was
not considered necessary or desirable in the present study,
since they might tend to obscure some of the physics of the
ocean problem.

e. Effects of coastline
   orientation

Solutions were obtained for three experiments identi-
cal to the one described in Section 3a except for the
orientation of the coastline. The orientation of the coast-
lines parallel to the direction of the wind stress are NE-SW,
SE-NW, and E-W. Except for the details of the wave solutions,
the results for the NE-SW and SE-NW coastline are almost
identical to the solution with a N-S coastline described in
Section 3a. Provided a Sverdrup interior is able to develop,
this is to be expected, since the primary effect of rotating
the coastline (plus the coordinate system and the direction
of the wind stress with it), is to change the value of β_y
acting to produce a pressure gradient in the direction of
the wind stress. In the rotated coordinate system $\beta_y = \frac{\partial f}{\partial y}$,
$\beta_x = \frac{\partial f}{\partial x}$, and both may be non-zero. As noted earlier for a
wind stress parallel to a meridional coast the magnitude of
the pressure gradient in the direction of the wind stress
wind stress parallel to a meridional coast the magnitude of
the pressure gradient in the direction of the wind stress
associated with a Sverdrup interior is essentially inde-
pendent of the value of β.

For a longshore-independent wind stress parallel to a zonal (y-coordinate) coastline, the Sverdrup vorticity constraint, (30), acts on the barotropic flow normal to the coast and the value of β_y acting to produce a longshore pressure gradient is zero. Hence, except for some of the oscillations, the coastal solution is similar to the f-plane solution of Case 7 in Section 3c. It is also in agreement with the two-dimensional solution for a zonal wind along a zonal coastline found by Kindle and O'Brien (1974), using a two-layer model. From their study Kindle and O'Brien concluded that a counter-undercurrent is unlikely along a zonal coast, but as noted earlier, the distribution of the wind stress and the proximity of boundaries may reduce the longshore barotropic mode sufficiently to permit the development of at least a weak counter-undercurrent.

4. EFFECTS OF LONGSHORE VARIATIONS IN BOTTOM TOPOGRAPHY

In this section we investigate the effects of long-shore variations in bottom topography on the time-dependent wind-driven eastern ocean circulation. Of special interest are the effects of the topography on the pattern of vertical motion and the associated baroclinic coastal jet. To the author's knowledge this particular time-dependent problem has not been subject to previous theoretical investigation. However, we may obtain some theoretical guidance from effects of topography on large scale uniform flows in the atmosphere and ocean. A priori, three dynamical concepts would appear to be especially helpful: conservation of potential vorticity, the equivalent β effect produced by sloping topography, and the joint effect of baroclinicity and bottom topography. The first suggests we should expect the flow to follow the isobaths. Recently, the third has been shown important in the steady state large scale ocean circulation by Sarkisyan (1969) and Sarkisyan and Ivanov (1971).

Rather than perform a detailed analysis of one solution where undue emphasis might be placed on dynamics relevant to a small class of problems, we will survey a number of solutions in Sections 4 and 5, attempting to identify vant to a small class of problems, we will survey a number of solutions in Sections 4 and 5, attempting to identify common characteristics and the important dynamical principles

43

involved in the time-dependent problem. This approach seems particularly appropriate in view of the meager literature (especially on time-dependent flows) from which we are able to draw support.

a. Effects of a wedge-shaped
   continental slope

The simplest interesting longshore topographic variation is a wedge-shaped continental slope. The effects of such topography have been investigated by means of two case studies with topography shown in Fig. 3. The wind stress is like that shown in Fig. 1, but with the half amplitude point 3150 km from the eastern boundary. $f_0 = 8.2 \times 10^{-5}$ sec^{-1}, $\Delta x = 2.5$ to 300 km, $\Delta y = 20$ km, and $\Delta t = 5$ min. Other parameters are given in the caption of Fig. 3 and in Table 2. The topographic value of β_T, determined from (33), is $(2.2$ to $7.7) \times 10^{-12}$ cm^{-1} sec^{-1} for Case a and $-(2.3$ to $7.3) \times 10^{-12}$ cm^{-1} sec^{-1} for Case b, an order of magnitude greater than that due to the earth's sphericity.

The salient features of the solutions are shown in Figs. 4 and 5. Fig. 4 shows v_2 at day 6 for Cases a and b. Note that the poleward undercurrent is well developed over the sloping topography where $\beta_T > 0$, but does not exist over the sloping topography where $\beta_T < 0$. Fig. 5 shows the vertically integrated x and y transport components for Cases a cally integrated x and y transport components for Cases a and b. This figure dramatically demonstrates that streamlines of the flow do not parallel the isobaths. Note also
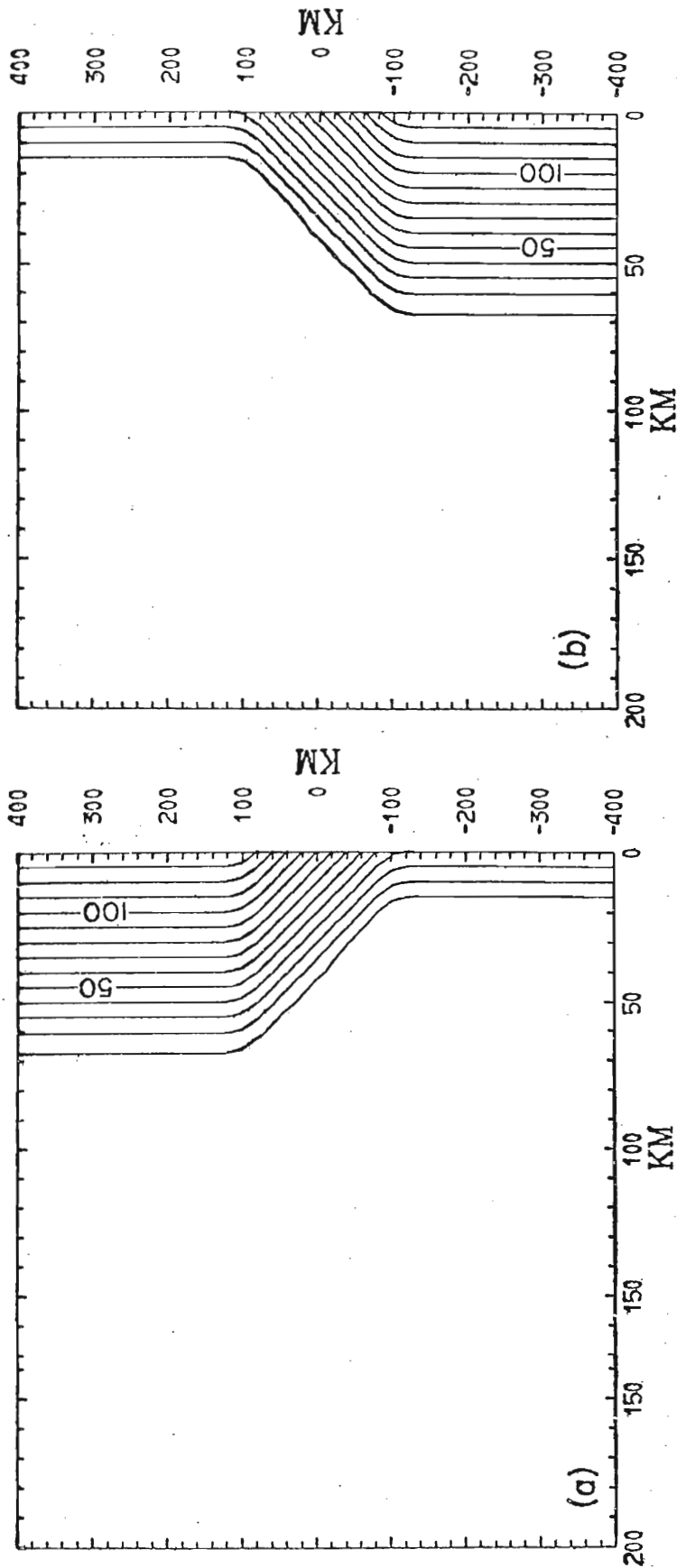
Fig. 3. Height of the bottom topography above a reference level in m for two cases with a wedge-shaped continental slope. The E-W continental slope is 2×10^{-3} and the magnitude of the N-S slope is 5×10^{-4}. The total model region is 6000×800 km.

Fig. 4. v_2 (cm sec^{-1}) at day 6 for Cases a and b. Note that the undercurrent in Case a extends through the region of N-S sloping topography, whereas in Case b it does not.

Fig. 5. The vertically-integrated x and y components of momentum in gm cm^{-1} sec^{-1} × 10^3 at day 6 for Cases a and b. Note that streamlines of the flow would not parallel the isobaths.

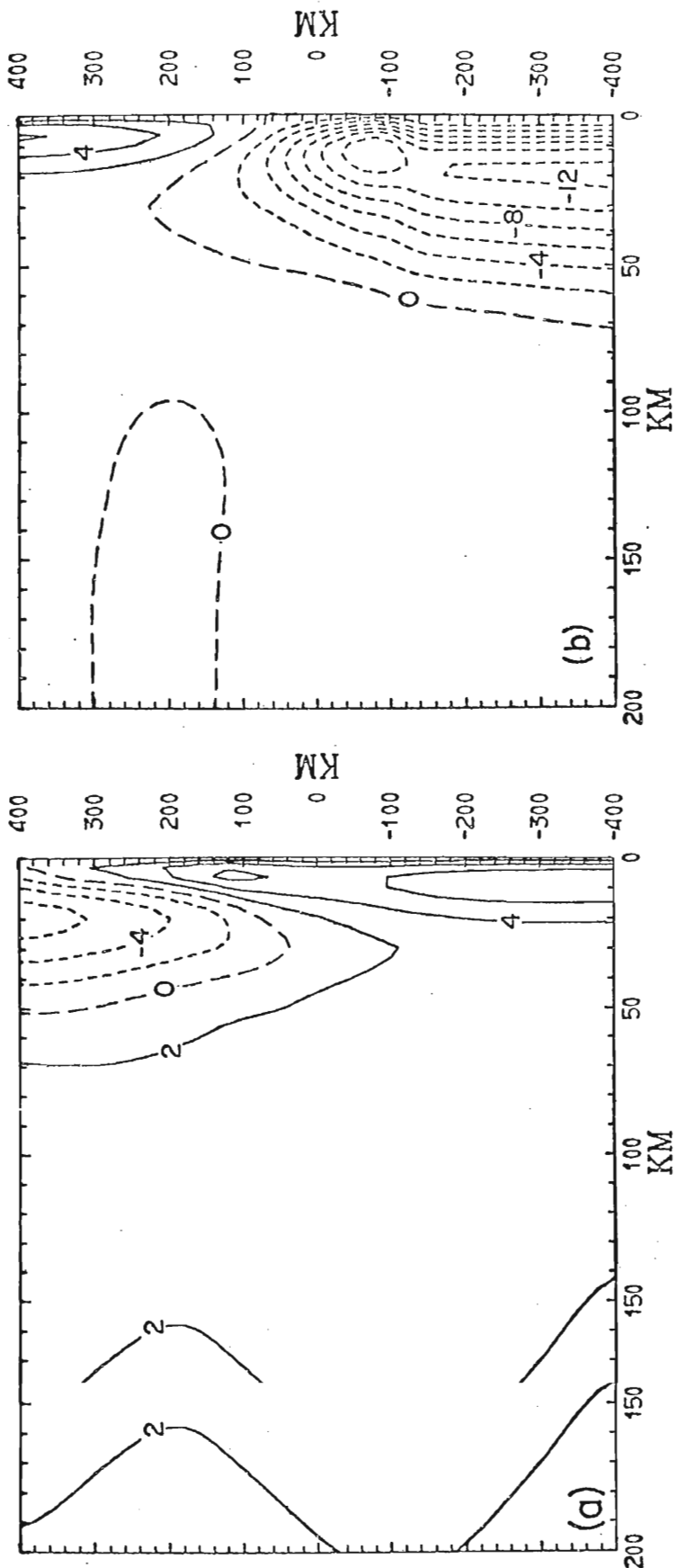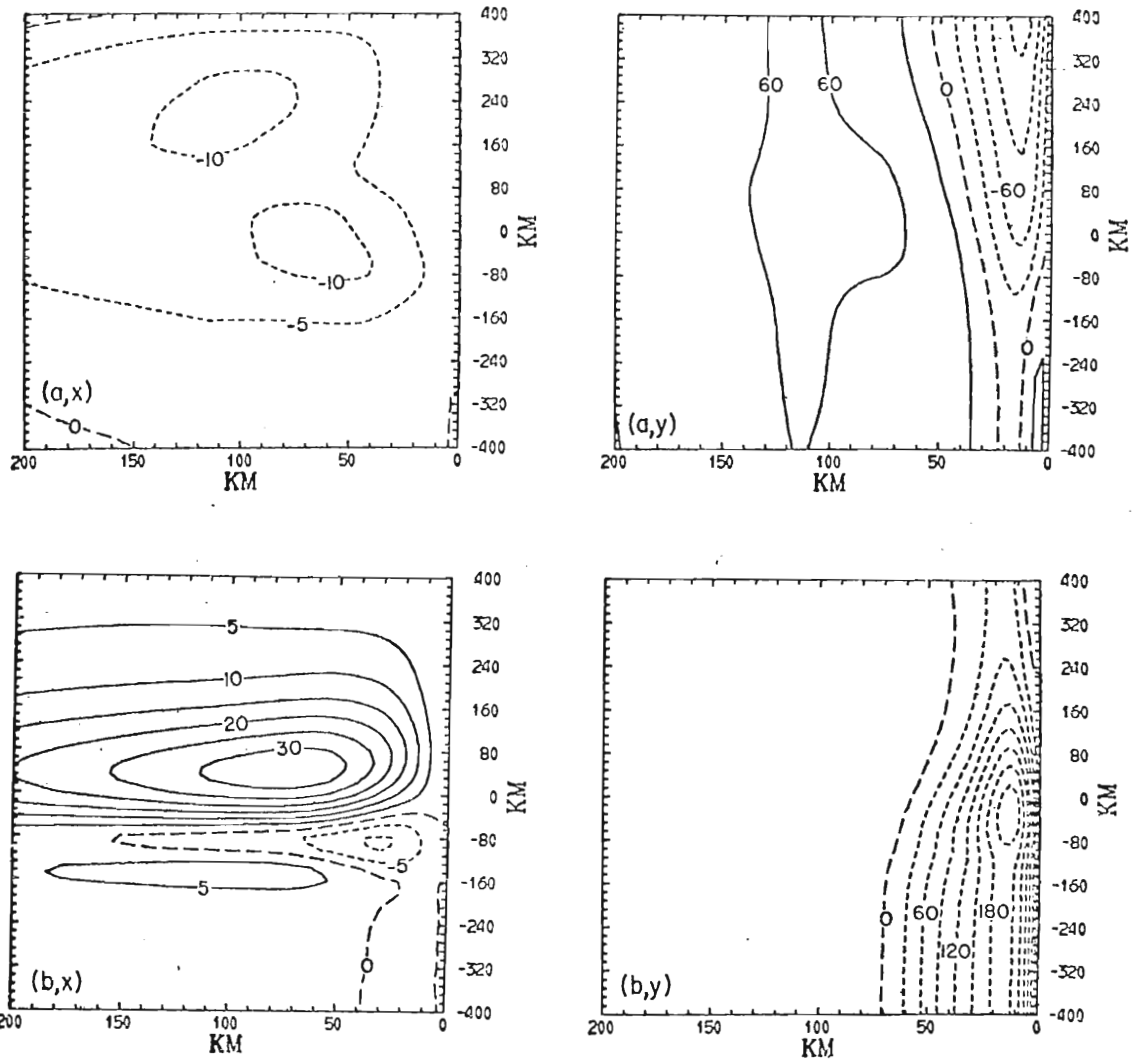that the combination of $\tau_{sy} < 0$ and E-W sloping topography causes potential vorticity to decrease following a fluid column, predicting a fluid column over the slope should move toward deeper water. In Case a, flow following the isobaths would give an onshore transport over the N-S sloping topography with a maximum of about 20000 gm cm^{-1} sec^{-1}; in Case b it would give offshore flow about -50000 gm cm^{-1} sec^{-1}. Furthermore, the character of the x-component differs greatly between the two cases. In Case b there is an onshore component with a maximum of about 35000 gm cm^{-1} sec^{-1} (1.7 cm sec^{-1}) with an E-W and N-S extent well beyond the limits of the sloping topography. The scale in both directions appears to be governed by the barotropic radius of deformation:

$$\lambda_E = \frac{[g(h_1 + h_2)]^{1/2}}{f} \tag{34}$$

The effect of the topography on the baroclinic mode (not shown) is less dramatic. The longshore component of this mode is weaker over the higher topography and stronger over the lower. The reason for this is explained in detail by Hurlburt and Thompson (1973). Because the baroclinic longshore flow is nearly geostrophic, its horizontal structure can be explained by the pattern of vertical motion. In brief, the upwelling at the coast over the lower topography is stronger than over the higher topography because in the in brief, the upwelling at the coast over the lower topography is stronger than over the higher topography because in the latter case greater upwelling occurs farther off shore induced by the sloping topography. This pattern of vertical

motion can be explained by conservation of potential vorti-
city in the upper layer. As required by mass continuity,
the total vertical transport in the upwelling region is
independent of the topography.

We will investigate the dynamics of the vertically
integrated transports by means of the following barotropic
equations:

$$\frac{\partial^2 v}{\partial x \partial t} + f \left(\frac{\partial u}{\partial x} + \frac{\partial v}{\partial y}\right) + \beta v = \frac{1}{\rho h} \frac{\partial \tau_{sy}}{\partial x} - \frac{\tau_{sy}}{\rho h^2} \frac{\partial h}{\partial x} \tag{35}$$

$$\frac{1}{h} \left(\frac{\partial h}{\partial t} + u \frac{\partial h}{\partial x} + v \frac{\partial h}{\partial y}\right) = - \left(\frac{\partial u}{\partial x} + \frac{\partial v}{\partial y}\right) \tag{36}$$

Note that the vorticity equation, (35), has been derived by
assuming geostrophy for the longshore flow, and by neglect-
ing advection and friction, except for the wind stress in the
y-momentum equation. The advective terms in the continuity
equation, (36), must be retained because of the sloping topo-
graphy. Substitution of (36) into (35) shows that the N-S
sloping topography yields a term analogous to the planetary
vorticity advection with β_T given by (33). Before we examine
the implications of this analogy more closely, let us assume
the analogy is exact and see what it implies about the
solution.

We noted earlier, (6), that β has an important effect
on the N-S pressure gradient, but that for planetary values
on the N-S pressure gradient, but that for planetary values
of β large scales, 0(1000 km), are necessary for this effect
to be important. However, the much larger values of β_T may

be important on the mesoscale, 0(100 km). We also noted
that E-W sloping topography normally leads to supergeostro-
phic onshore flow in the lower layer and a barotropic accele-
ration in the direction of the wind stress. Thus, with $\beta_T > 0$
we might expect v_2 to exhibit equatorward flow over the
western portion of the E-W and N-S sloping topography, but a
poleward current might be expected closer to shore as observed
in Fig. 4a. For $\beta_T < 0$ we would expect v_2 to exhibit stronger
equatorward flow over the E-W and N-S sloping topography than
if there were no N-S slope. Again this is observed in Fig.
4b. We would also expect the v-component of the vertically-
integrated flow to exhibit similar characteristics, although
perhaps not the nearshore poleward flow. This is verified
in Figs. 5a,y; b,y. The patterns for the u-component (Figs.
5a,x; b,x) are consistent with the requirements of mass con-
tinuity for the longshore flow. Not surprisingly, the funda-
mental scale governing this time-dependent flow appears to
be the barotropic radius of deformation. Effects of the topo-
graphy on the baroclinic u-component (not shown) are obscured
by inertial oscillations, and in this case no attempt has
been made to filter out these oscillations.

The concept of the topographically-induced β effect
has proved very successful at explaining the observed
features of the flow, but before continuing to more compli-

features of the flow, but before continuing to more compli-
cated topography, let us re-examine the implications of this
analogy in terms of (35) and (36). Recall that derivation

of the relation between planetary vorticity advection and the N-S pressure gradient requires integration of (35) with respect to x. This tells us that for the topographic β analogy to be complete, we must have

$$\frac{v}{h} \frac{\partial h}{\partial y} \simeq - \frac{\partial v}{\partial y} \tag{37}$$

Eq. (37) is a constraint on the longshore horizontal divergence by N-S sloping topography. As we have seen from (31), $f(\partial v/\partial y)$ is potentially an important contributing factor to the N-S pressure gradient in some situations, and it is in this way that the topographic β analogy may be completed. By converting to velocities, taking into account the local depth, we can see that the longshore components in Fig. 5 are in good agreement with (37).

b. Effects of a mesoscale canyon

To investigate additional effects of topography, a case with topography resembling a mesoscale canyon-like feature off the Oregon coast (Fig. 6), was driven by an equatorward wind stress like that used for the cases discussed in Section 4a. The wind was shut off at day 5. $H_1 = 30$ m, $\Delta x = 2.5$ to 300 km, $\Delta y = 10.7$ to 56 km and $\Delta t = 3$ min. Other parameters are given in the caption of Fig. 6 and in Table 2. The topographic depression exhibits a significant and complex effect on the flow, the salient and in Table 2. The topographic depression exhibits a significant and complex effect on the flow, the salient characteristics of which will be described in comparison to a solution for a y-independent continental slope, i.e., in
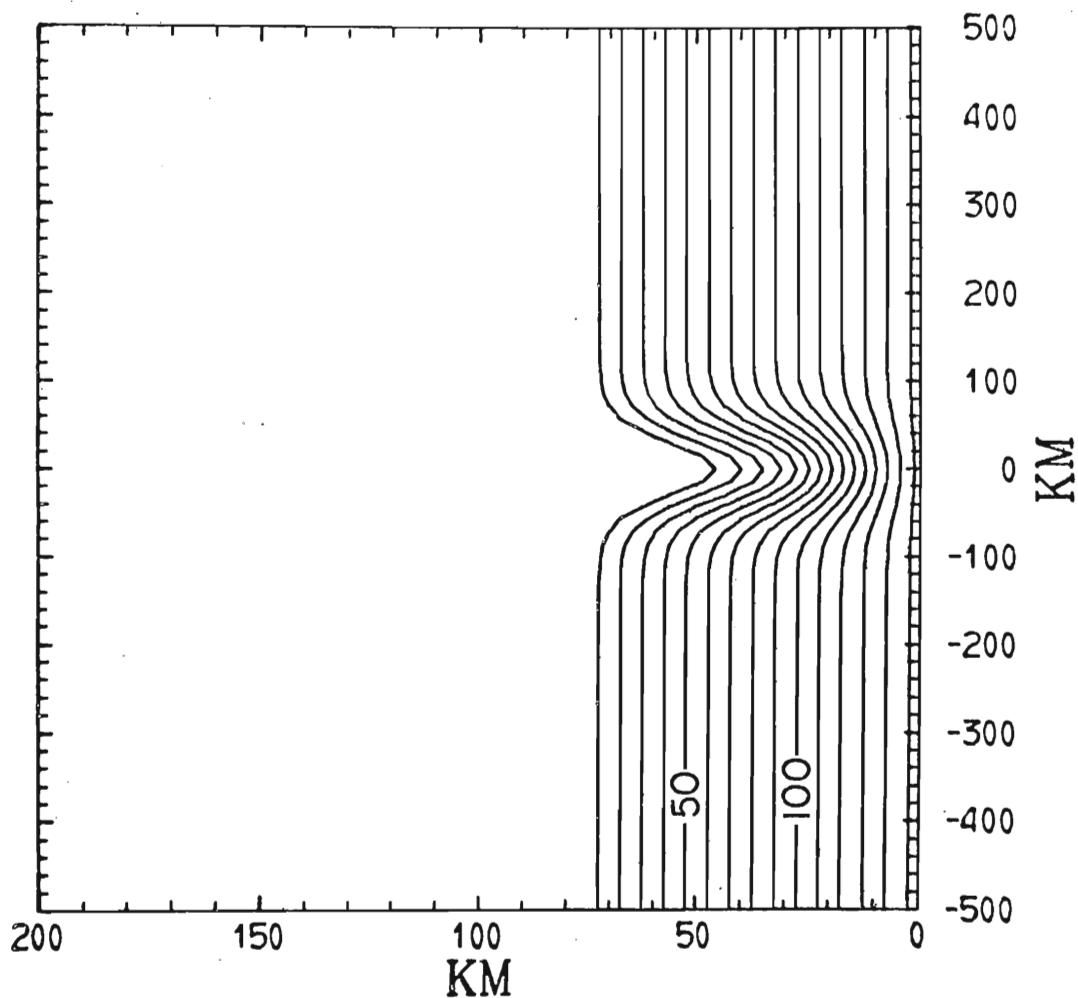
Fig. 6. Height of the bottom topography above a reference level in m for a case with topography resembling a canyon-like feature off the Oregon coast. The E-W continental slope is 2×10^{-3}. The N-S and E-W profiles of the canyon are governed by a normal probability density function. The standard deviation for the N-S profile is 35 km with a maximum amplitude of 55 m 40 km off shore and zero amplitude at the coast. The total model region is 6000×1000 km.

terms of canyon minus no canyon. The subtraction of these
two solutions not only clearly defines the effects of the
depression, but also filters out most inertial oscillations,
Rossby waves, and gravity waves which might otherwise obscure
some effects of the canyon.

The solution in terms of canyon minus no canyon is
shown in Figs. 7-9. The baroclinic transports are the de-
parture from the barotropic transport in each layer. Both
the maximum residual barotropic and baroclinic transports
correspond to maximum speeds of about 1 cm sec^{-1} for the flow
normal to the coast and 4 cm sec^{-1} for the longshore flow.
Thus, the velocity normal to the coast induced by the canyon
is the same order as the subsurface flow required to compen-
sate the Ekman drift. At day 5 the total longshore flow
consists of a baroclinic component with a maximum speed of
approximately 30 cm sec^{-1} and an equatorward barotropic
component with a maximum speed of 12.5 cm sec^{-1}. No pole-
ward undercurrent formed in the course of the integration.

At both days 5 and 10 the lower layer transports look
much like the barotropic transport. Thus, only the upper
layer transports are shown in Fig. 8. At day 5 the residual
(i.e., canyon minus no canyon) circulation (Fig. 7a) exhibits
a highly asymmetric two-cell pattern divided along the axis
of the canyon in both the barotropic and lower layer trans-
of the canyon in both the barotropic and lower layer trans-
ports. The larger scale upwind cyclonic cell (centered at
95, 60) is barotropic and its scale appears to be influenced
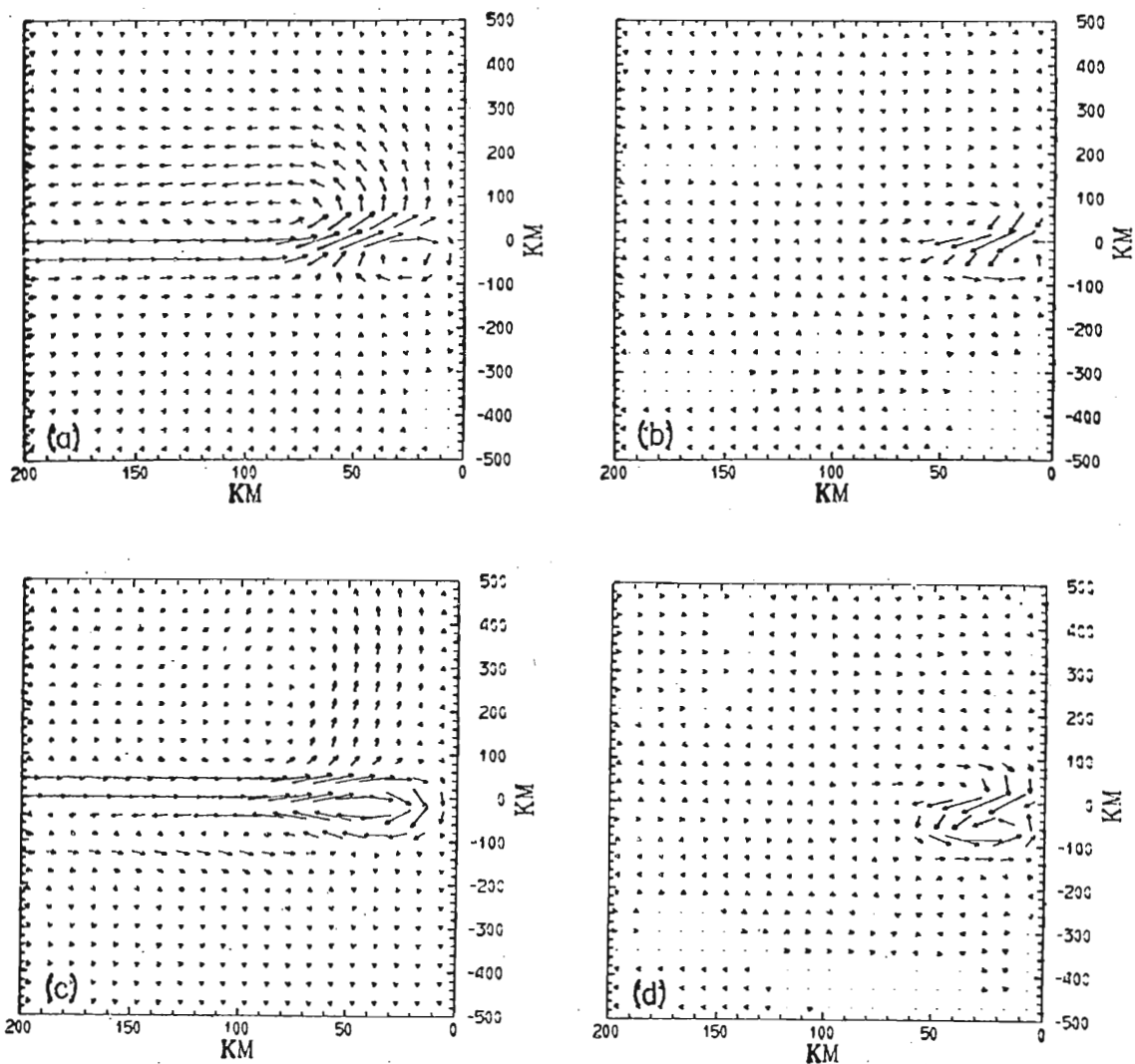
Fig. 7. Barotropic (a,c) and baroclinic (b,d) transports at days 5 (a,b) and 10 (c,d) in terms of canyon minus no canyon. The direction of the arrows for the baroclinic transport is for the upper layer. The length of the arrows is scaled by the longest arrow on each frame. The wind was shut off at day 5. The arrows define streamlines, not geographical direction in this and the other vector plots, i.e., the x-component is multiplied by 1000/200 = 5.

not geographical direction in this and the other vector plots, i.e., the x-component is multiplied by 1000/200 = 5.
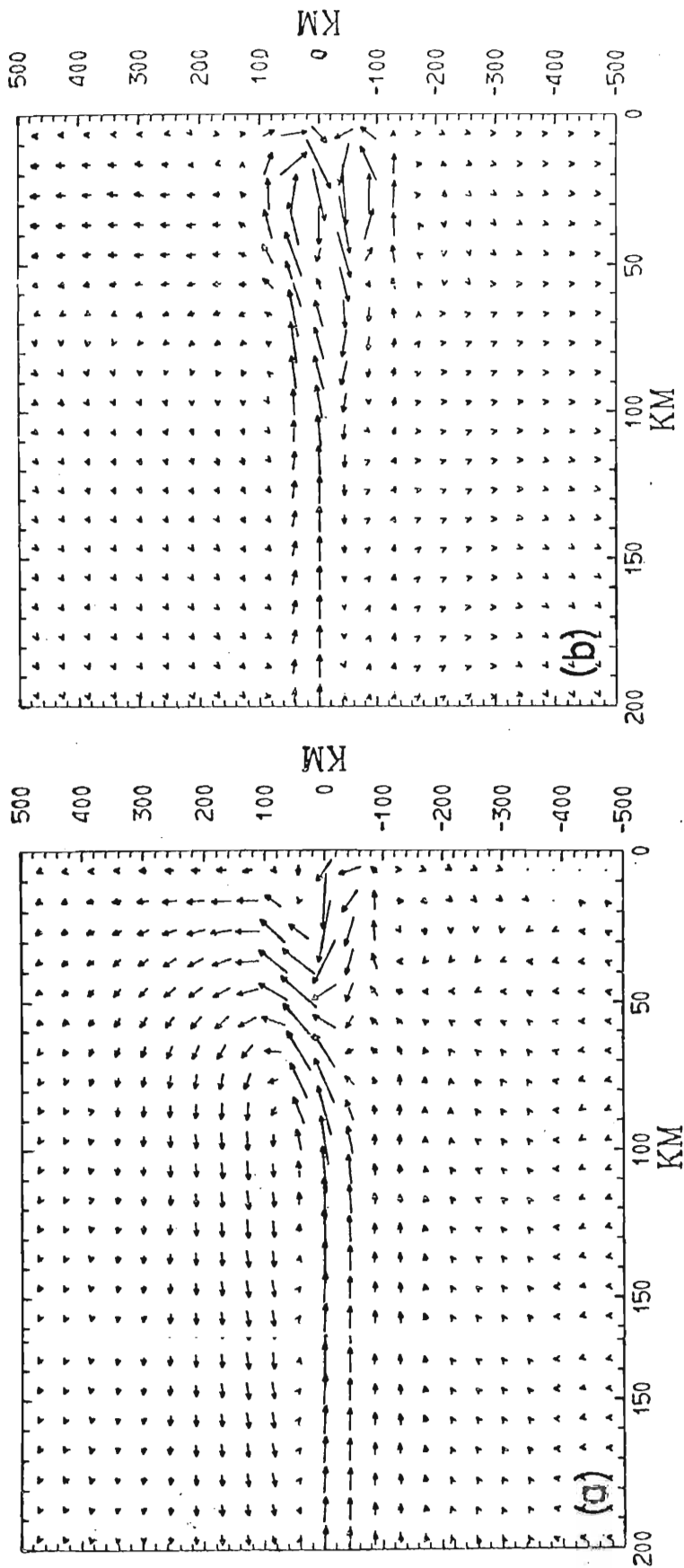
Fig. 8. Residual upper-layer transports at days
5(a) and 10(b). The length of the arrows is scaled by the
longest arrow on each frame in this and other figures. The
lower layer transports are much like the barotropic trans-
ports. The wind was shut off at day 5.
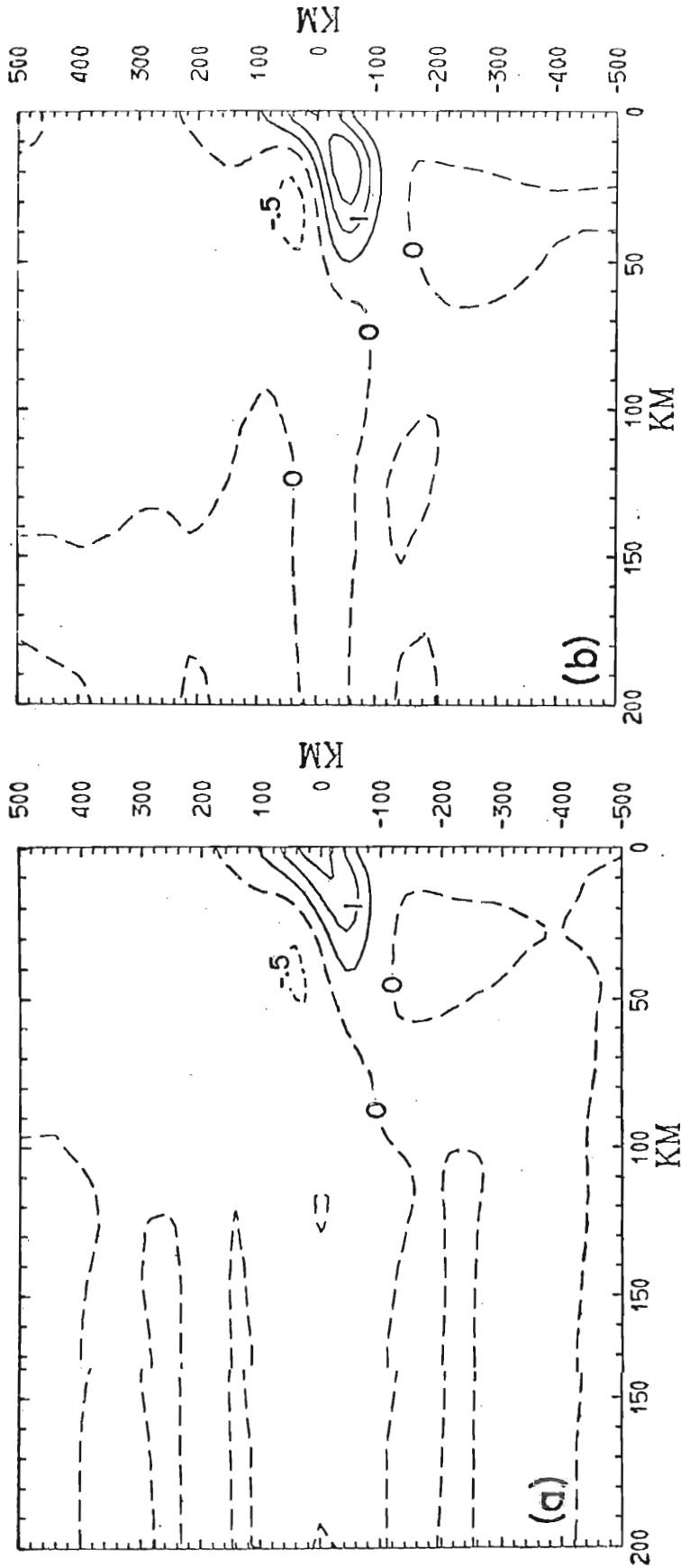
Fig. 9. Residual pycnocline height anomaly in m at days 5(a) and 10(b). Note the upwelling is decreased on the north side of the canyon and is enhanced on the south side and near the coast on the axis of the depression.

primarily by the barotropic radius of deformation and second-
arily by the scale of the canyon. The smaller scale downwind
cell is cyclonic in the upper layer (Fig. 8a) and anticyclonic
in the lower layer (Fig. 7a). Its scale appears to be govern-
ed by the scale of the canyon. The barotropic contribution
is centered at -x = 30 km, y = -30 km (Fig. 7a). The baro-
clinic contribution (centered at 15, -50) dominates in the
upper layer and is cyclonic there (Fig. 7b). There is also
a weaker baroclinic cell anticyclonic in the upper layer
north of the canyon axis centered at 45, 50.

By day 10 (after the winds have been shut off for
5 days) the large scale, barotropic, cyclonic cell (now
centered at 85, 220) has propagated northward at a speed of
40 cm sec^{-1} and become much weaker. The strength of the
smaller scale barotropic anticyclonic cell (now centered at
45, -25) is virtually unchanged (Fig. 7c). The southern
baroclinic cell (now centered at 20, -60) has intensified
(Fig. 7d) and combined with the barotropic cell produces
the remarkable two-cell pattern in the upper layer (Fig.
8b) with a col centered over the single anticyclonic cell
in the lower layer (Fig. 7c).

Fig. 9 shows the residual pycnocline height anomaly
after 5 (Fig. 9a) and 10 (Fig. 9b) days. The upwelling is
decreased on the north side of the canyon and enhanced on
decreased on the north side of the canyon and enhanced on
the south side and near the coast on the axis of the canyon.
The pattern for the baroclinic component in the upper layer

is similar to the pattern for $\vec{V}_1 - \vec{V}_2$. Note that the residual patterns for the baroclinic component (Fig. 7b,d) are in general geostrophic agreement with the residual patterns of the pycnocline height anomaly. The enhanced upwelling near the coast can be explained by the steeper E-W slope in this region and conservation of potential vorticity in the upper layer (e.g., see Hurlburt and Thompson, 1973 and Section 4a). The N-S pattern of the upwelling is inconsistent with conservation of potential vorticity in the upper layer:

$$\frac{\partial v_1}{\partial x} - \frac{\partial u_1}{\partial y} = f \left(\frac{h_1 - H_1}{H_1} \right) \qquad (38)$$

However, it is consistent with the topographic β effect discussed in Section 4a, which requires a stronger N-S pressure gradient north and a weaker N-S pressure gradient south of the canyon axis. The barotropic poleward residual north and equatorward residual south of the canyon axis (Fig. 7a) are also consistent with the topographic β effect. The divergent nature of these two components and mass continuity require the barotropic onshore flow on the axis of the canyon. The broad outflow for both branches occurs to the NW of the canyon. The residual circulation centered 30 km SSE of the center of the canyon appears to be a distorted attempt by the flow to follow contours of canyon minus no canyon. This attempt improves by day 10 (after

minus no canyon. This attempt improves by day 10 (after the winds have been shut off for 5 days) when the large circulation cell has propagated north and decreased in

strength, and the smaller cell is centered 25 km SSW of the center of the canyon. The residual cellular structure appears wave-like in the total barotropic flow shown in Fig. 10, and the distortion in the attempt of the nearshore flow to follow the contours of topography by the larger scale wave is clearly evident.

c. Effects of a mesoscale ridge

A case with the ridge topography shown in Fig. 11 was integrated for comparison with the effects of the canyon. Except for the topography all the model parameters are the same as for the canyon. Except in the western part, contours of canyon minus no canyon are the negative of ridge minus no ridge. Since the dynamical principles involved are similar to those applicable in the cases discussed in Sections 4a and 4b, only a brief description of the solution for a ridge will be given.

Fig. 12 shows the barotropic residual (ridge minus no ridge) transport at day 5. In this case the cell (centered at 40, -15) following contours of ridge minus no ridge dominates the flow. A circulation with an E-W scale which appears to be governed by the barotropic radius of deformation, (34), still exists, but the dominant N-S scale is the scale of the ridge, a characteristic which occurred only at day 10 (after the winds had been shut off 5 days) in the case of the canyon. An anticyclonic cell with a N-S

Fig. 10.   Total barotropic transport at day 2.25. Day 2.25 was chosen because it is least contaminated by Rossby waves.
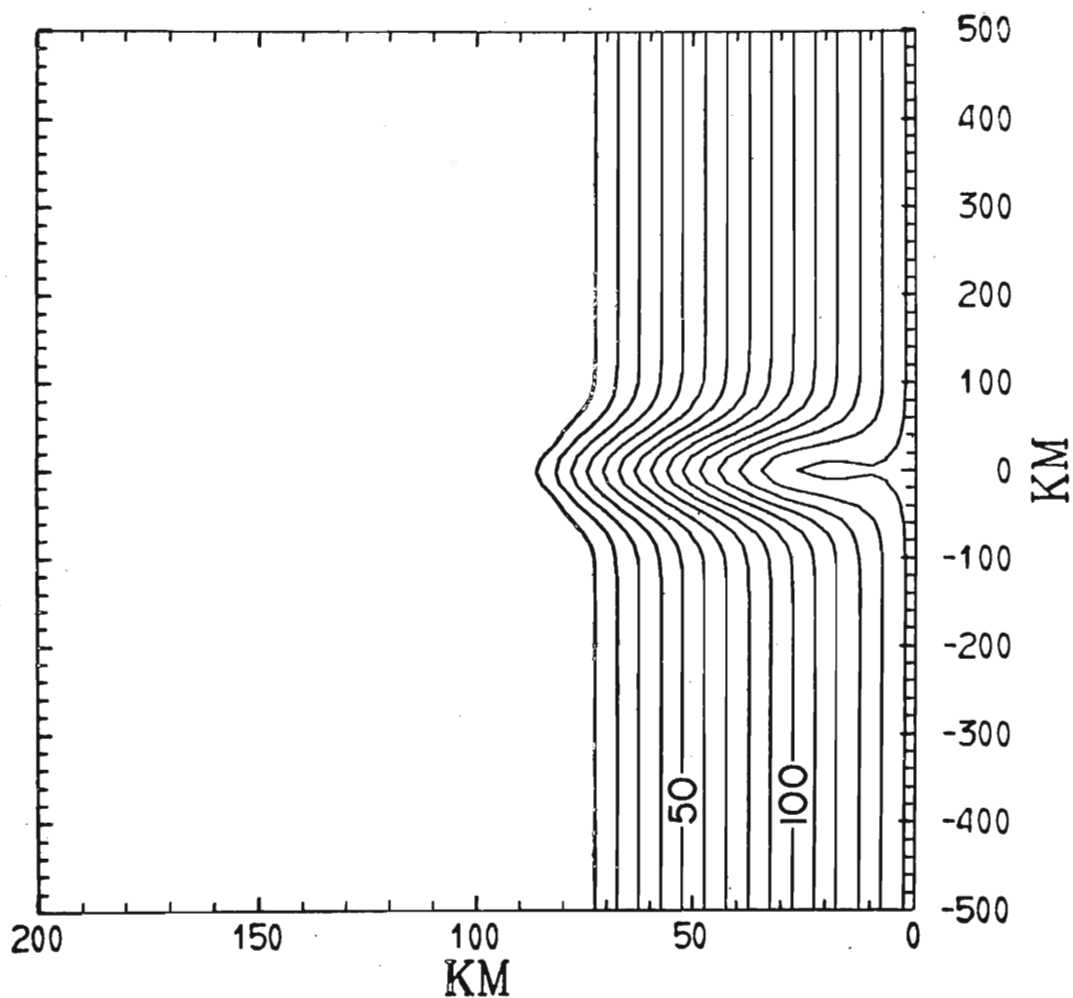
Fig. 11. Height of the bottom topography above a reference level in m for a case with a ridge superimposed on a continental slope. The E-W continental slope is 2×10^{-3}. The N-S and E-W profiles of the ridge are governed by a normal probability density function. The standard deviation for the N-S profile is 35 km with a maximum amplitude of 55 m 40 km off shore and zero amplitude at the coast. Contours of canyon minus no canyon are the negative of ridge minus no ridge except in the western portion.

tude of 55 m 40 km off shore and zero amplitude at the coast. Contours of canyon minus no canyon are the negative of ridge minus no ridge except in the western portion.
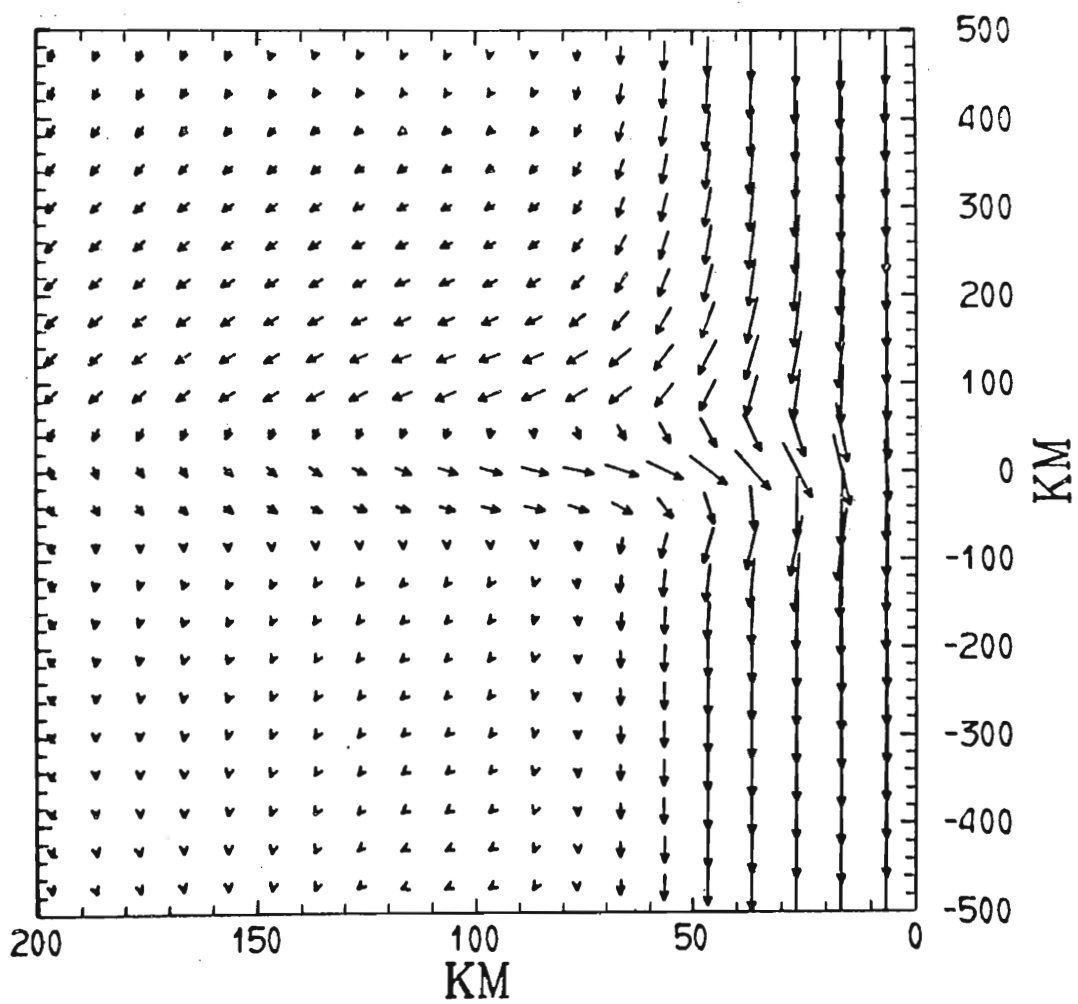
Fig.12. (a) Residual (ridge minus no ridge) barotropic transport at day 5. (b) Total barotropic transport at day 2.25. Day 2.25 was chosen because it is least contaminated by Rossby waves.

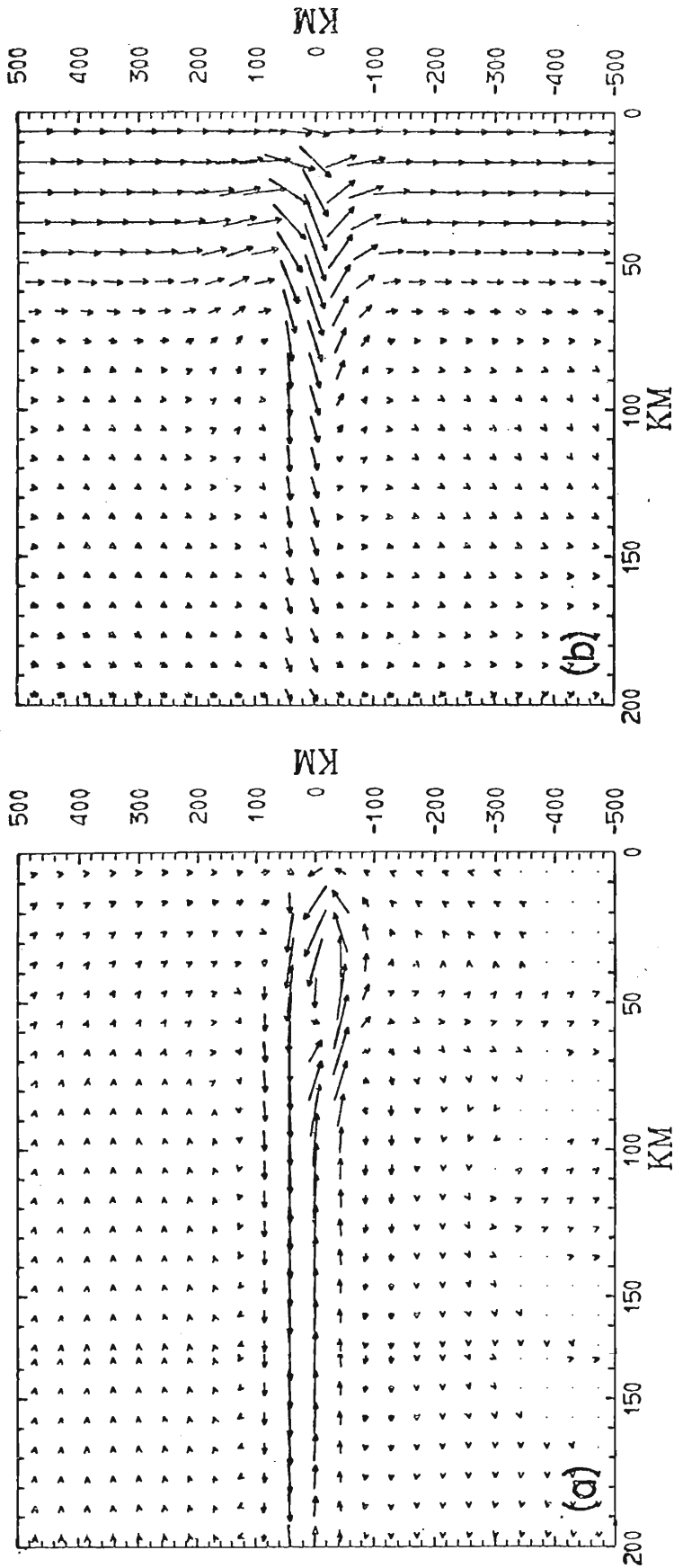extent which appears to be governed by the barotropic radius of deformation does exist, but it is very weak.

For comparison, Fig. 12b shows the total barotropic transport. This time the part of the wave north of the ridge is weak and the part at the latitude of the ridge is strong and extends well beyond the ridge. This is opposite the canyon case. Quite striking in all the solutions with longshore variations in topography is the lack of noticeable wave phenomena associated with the topographic perturbations except for the single cycle wave-like feature shown in Figs. 10 and 12b, and the northward propagation, after the wind has been turned off, of the large scale barotropic cell in the residual flow north of the canyon.

Fig. 13a shows the residual pycnocline height anomaly at day 5 with enhanced upwelling north and decreased upwelling south of the ridge. The regions of greatest pycnocline anomaly are confined to the region of the barotropic equator-ward current, although the ridge extends well beyond the current. The dynamics of the anomalies are consistent with those of the cases discussed in Sections 4a and 4b. Note that the residual of $\vec{V}_1 - \vec{V}_2$ (Fig. 13b) is in excellent geostrophic agreement with the residual pycnocline height anomaly.

The basic flows are the same as for the canyon, but anomaly.

The basic flows are the same as for the canyon, but the residual flows are stronger, up to 4 cm sec^{-1} normal to the coast and 7 cm sec^{-1} longshore. No poleward undercurrent
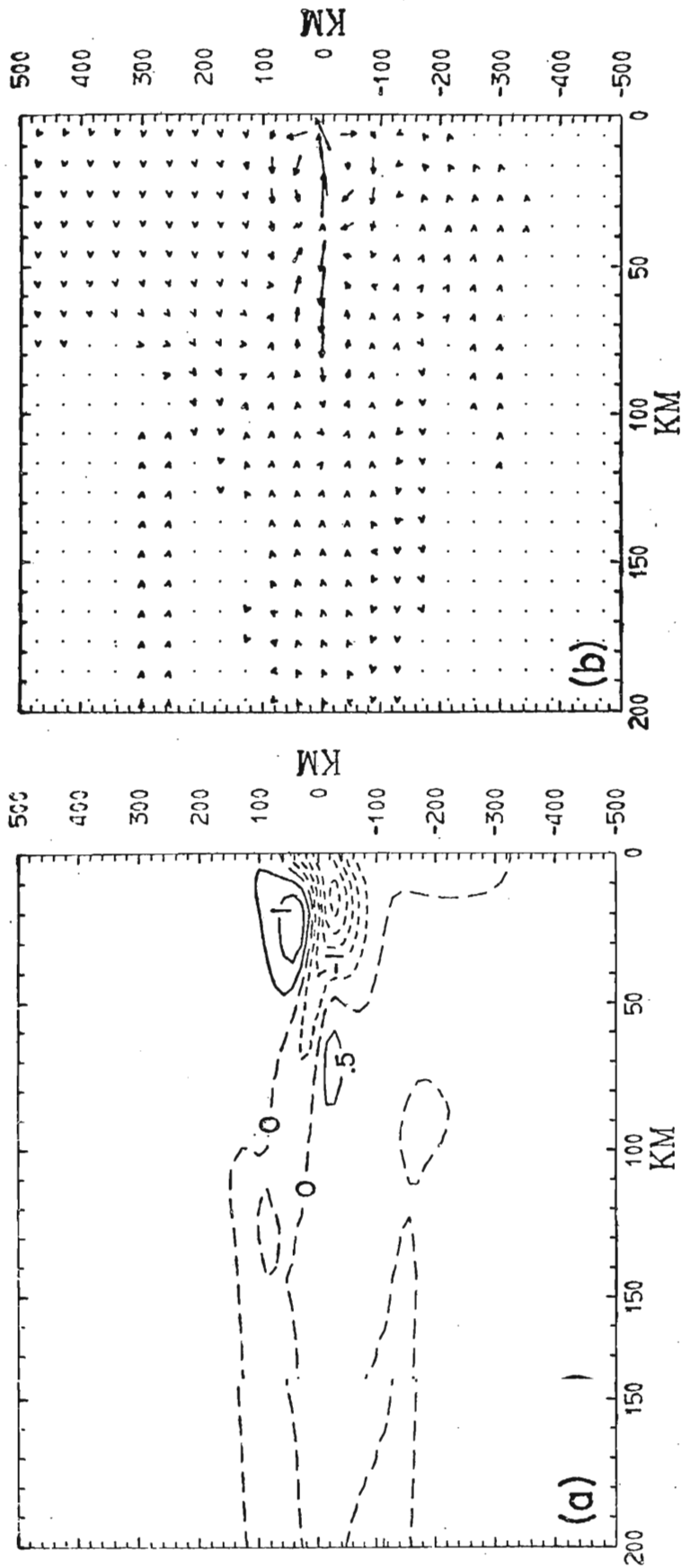
Fig. 13. Residual pycnocline height anomaly (a) and the residual of $\vec{V}_1 - \vec{V}_2$ (b) at day 5. Note that the patterns are in excellent geostrophic agreement.

forms in the course of the integration except in a region within 10 km of the coast with a longshore extent of 100 km on the south side of the ridge. The maximum poleward flow is about 3 cm sec^{-1} at day 5.

5. EFFECTS OF COASTLINE GEOMETRY

The effects of coastline geometry have been investigated by means of case studies utilizing the coastline configurations shown in Fig. 14. The model was driven from rest or from the quasi-balanced initial state described in Section 2c by the equatorward, y-independent wind stress shown in Fig. 1. All six cases were integrated twice, once from each initial state. In Cases a and b Δx = 4 to 300 km; in Cases c through f Δx = 3 to 300 km. Δx versus x for Cases a and b is given in Table 1. In Cases d, e, and f Δy = 5 to 60 km, and L_y = 1000 km. The E-W dashed lines over the land in Fig. 14 and other figures in this section indicate grid rows in y. In all six cases Δt = 1.5 min. The other model parameters are given in Table 2 except that in Case f, H_1 = 30 m.

a. Effects of a corner

Since it was feasible to resolve the baroclinic radius of deformation along a section of zonal coastline by using stretch coordinates in the y-direction, Cases a and b were chosen as best able to clearly depict the effects of coastline geometry. Some interesting very small scale (< 10 km) nonlinear effects are not resolved by the 4 by 5 km

grid mesh used in the vicinity of the corner, but the geostrophically balanced phenomena are adequately represented.
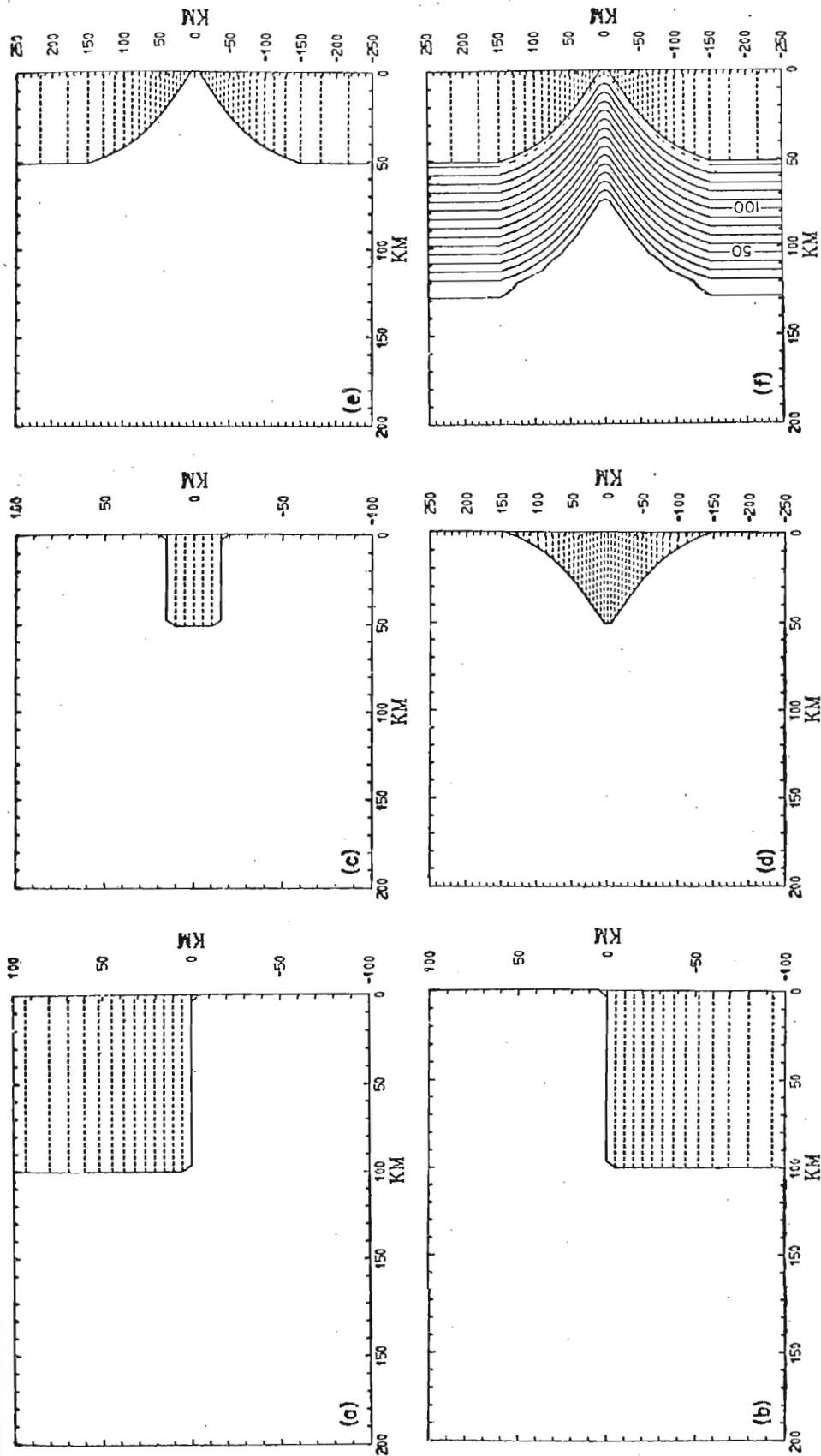
66

67

Fig. 14. Coastline configurations used to investigate the effects of coastline irregularities on the wind-driven eastern ocean circulation. In Cases a through e the bottom topography is flat. In Case f the topography follows the coastline with a uniform E-W slope of 2×10^{-3}. The topography rises to 155 m above the reference level at the coast.

Of principal interest are the patterns of horizontal and vertical motion near the corners and along the section of zonal coastline where the wind stress is normal to the coast. The two-dimensional (longshore-independent) problem demonstrates that a steady wind stress normal to the coast drives vertical motion on the f^{-1} time scale, and thus produces little vertical transport. The associated longshore currents are more than an order of magnitude weaker than those associated with longshore winds. Hence, the manner in which the barotropic and baroclinic modes of the coastal currents conserve mass is of key interest. If the baroclinic mode conserved mass in a vertical plane, then for Case a and an equatorward wind stress we should expect enhanced upwelling near the eastern end of the zonal segment and decreased upwelling near the western end. If the baroclinic mode conserves mass in a horizontal plane, then geostrophic balance of this component implies strong upwelling not driven directly by the wind along the E-W segment of the coastline. That is, horizontal conservation means currents along the two meridional segments of coastline are connected by currents along the zonal segment; conservation in a vertical plane implies the absence of connecting currents along the zonal segment. Other items of interest include possible formation of flow instabilities and eddies, possible boundary layer separation of of interest include possible formation of flow instabilities and eddies, possible boundary layer separation of zonal current segments, and the occurrence of large

amplitude wave phenomena. The latter were notably absent in the presence of longshore variations in bottom topography.

Fig. 15a,b shows the pycnocline height anomaly for Case a at day 5. The solution in Fig. 15a was driven from rest, the one in Fig. 15b from the quasi-balanced initial state. The low frequency part of the solutions from the two initial states are virtually identical, but the numerical solutions demonstrate that the quasi-balanced initial state reduces the amplitude of the inertial oscillations, Rossby waves, and gravity waves by up to three orders of magnitude.

More important, however, Fig. 15 shows that strong upwelling occurs along the zonal section of the coast. This upwelling cannot be driven directly by the wind, which is offshore along this segment. Fig. 15 also shows that the upwelling is greater at the eastern end of the segment than at the western end. Fig. 16 shows that the equatorward surface jet and poleward undercurrent follow the coastline consistent with Fig. 15 and geostrophic balance.

The basic dynamics of the baroclinic mode can be understood by examination of the following reduced gravity model:

$$\frac{\partial u_1}{\partial t} - f v_1 = - g' \frac{\partial h_1}{\partial x} \tag{39}$$

$$\frac{\partial v_1}{\partial t} + f u_1 = - g' \frac{\partial h_1}{\partial y} + \frac{\tau_{sy}}{\rho h_1} \tag{40}$$

$$\frac{\partial v_1}{\partial t} + f u_1 = - g' \frac{\partial u_1}{\partial y} + \frac{\tau_{sy}}{\rho h_1} \tag{40}$$

$$\frac{\partial h_1}{\partial t} + h_1 \left(\frac{\partial u_1}{\partial x} + \frac{\partial v_1}{\partial y} \right) = 0 \tag{41}$$
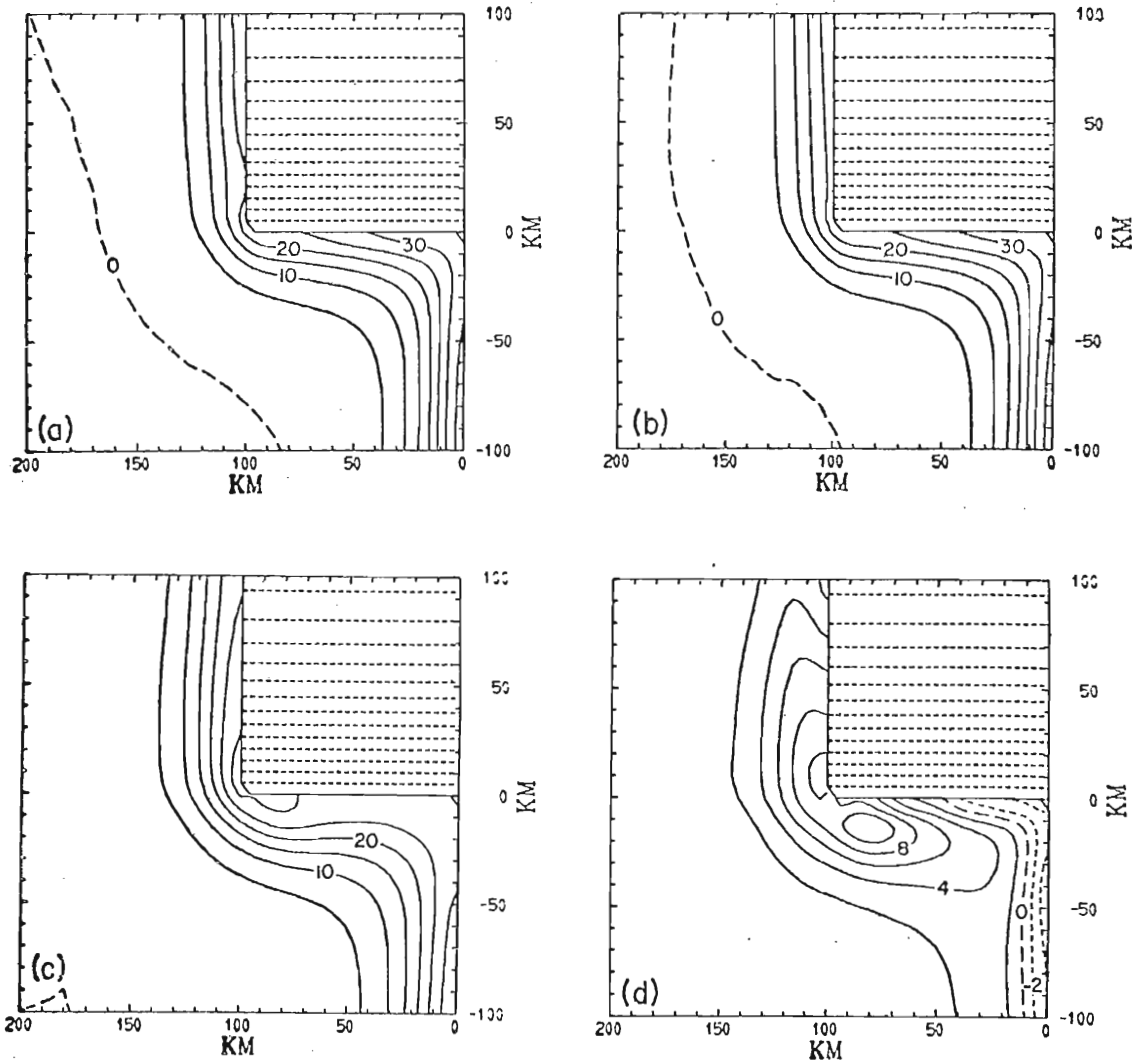
Fig. 15. Pycnocline height anomaly in m at day 5 for a solution driven from rest (a) and from a quasi-balanced state (b). The pycnocline anomaly at day 10 (c) was driven from the quasi-balanced state, but the wind was shut off at day 5. (d) is the pycnocline height anomaly at day 10 minus that at day 5.
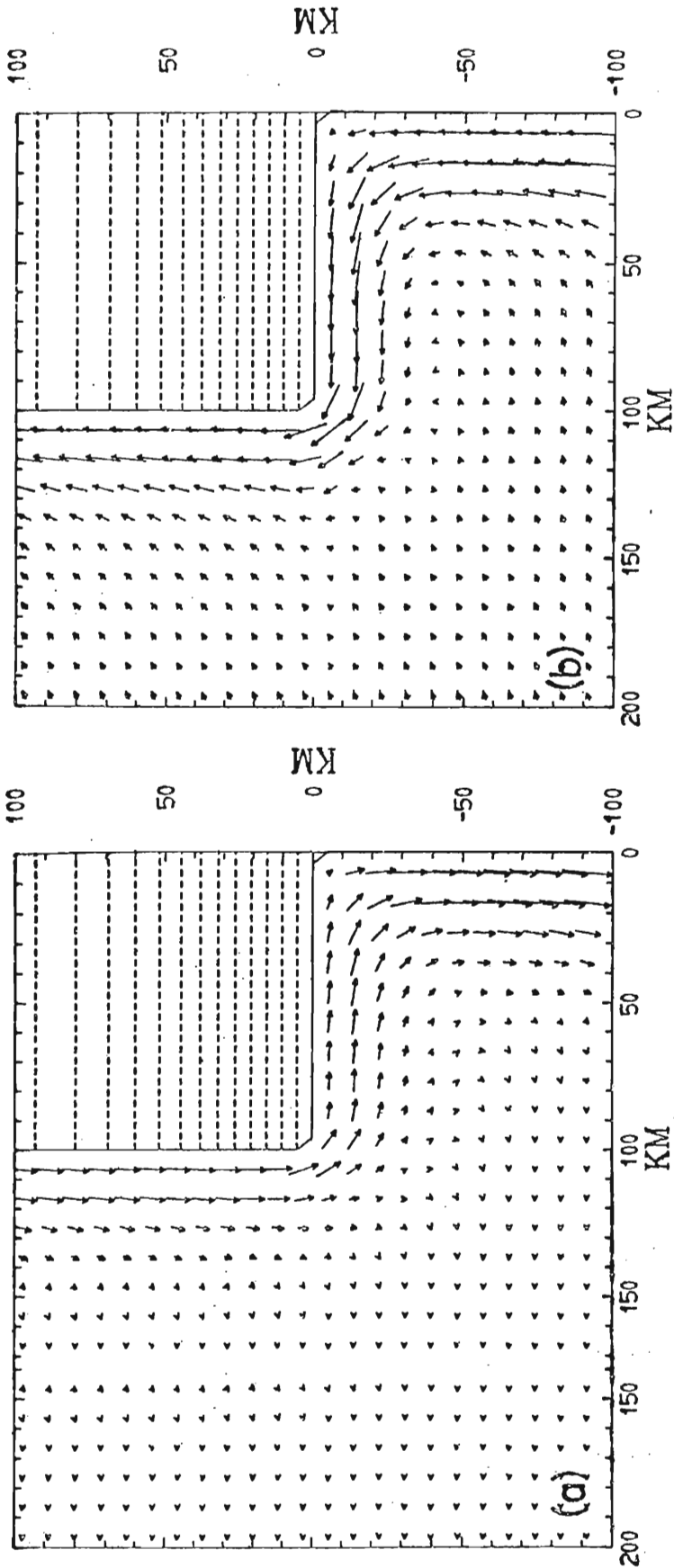
Fig. 16. Upper layer velocity (a) and lower layer velocity (b) for Case a at day 5. Note that the currents follow the coast and are oppositely directed.

where $u_2 = v_2 = 0$, and $h_2 = \infty$. The necessity for the zonal current segment can be demonstrated by considering mass continuity of the coastal jets in a y-z plane. Since $v_1 \rightarrow 0$ near the eastern end of the zonal segment to satisfy the kinematic boundary condition, mass continuity in a y-z plane would require $\partial v_1/\partial y > 0$ and $\partial u_1/\partial x > 0$ near this corner. Thus, both (40) and (41) would demand greatly enhanced up-welling near the eastern end of the zonal segment. However, geostrophic balance in (39) is not possible in this region. Hence, $\partial u_1/\partial t > 0$ and a zonal current segment must be present. Note that if $\tau_{sy} \rightarrow 0$ at the zonal segment on a scale greater than the baroclinic radius of deformation, the zonal current segment is no longer required.

Although we have demonstrated the necessity for a zonal current segment, the enhanced upwelling at the eastern end of the segment and reduced upwelling at the western end show that a vertical circulation is present. Thus, the flow required by mass continuity is partitioned between the horizontal and vertical circulations. The westward decrease of the upwelling along the zonal segment also shows that the E-W extent of any zonal current must be limited, and would not extend the length of a long, O(1000 km) or more, zonal coastline segment.

Fig. 15c,d and Fig. 17 demonstrate the importance of Kelvin wave dynamics in the presence of coastline irregu-
Fig. 15c,d and Fig. 17 demonstrate the importance of Kelvin wave dynamics in the presence of coastline irregu-larities. Fig. 17a,b shows the northward propagation (at
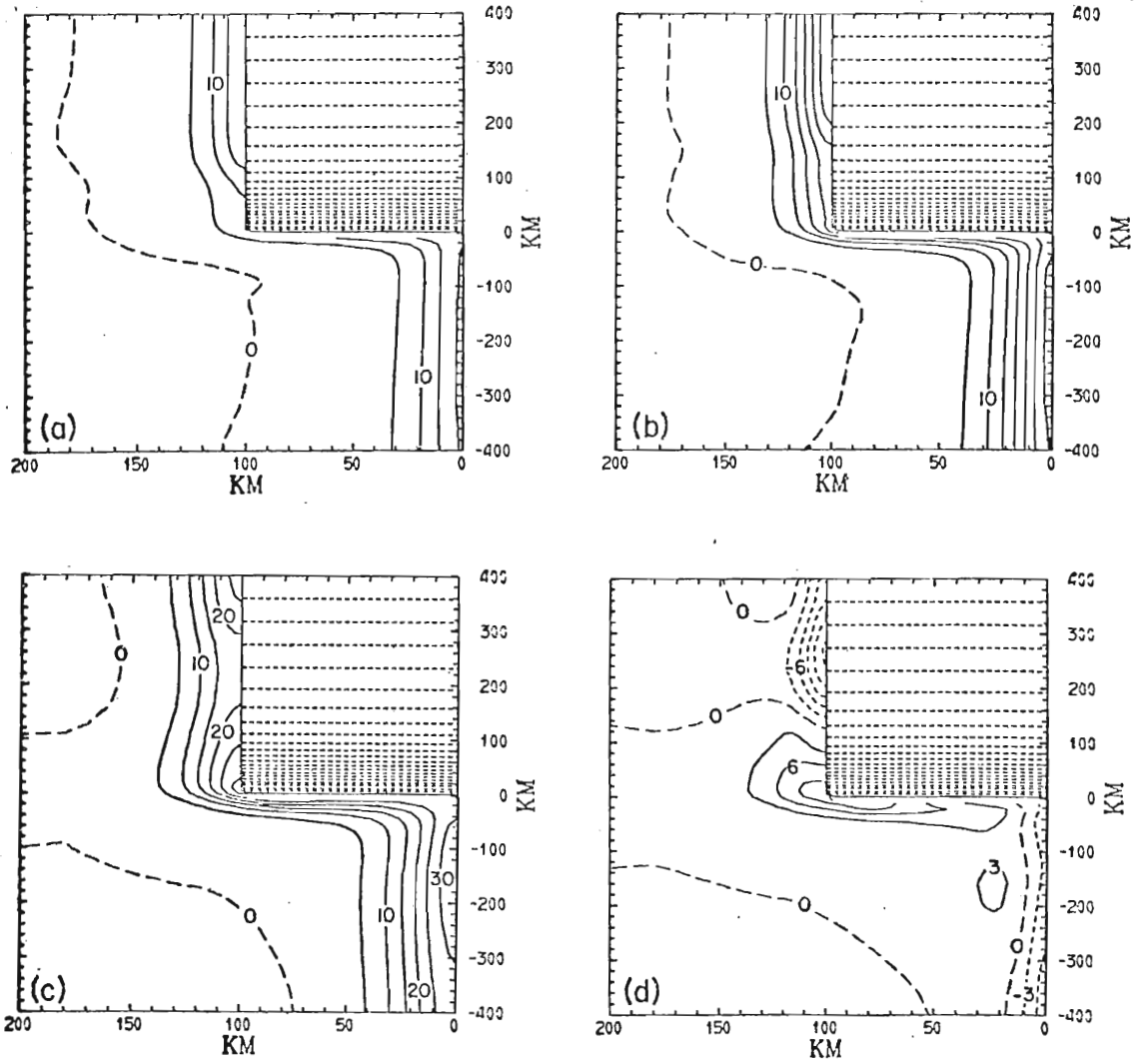
Fig. 17. Pycnocline height anomaly in m for the entire N-S extent of the model region at day 3 (a), 5 (b), and 10 (c). The wind was shut off at day 5. (d) is the pycnocline anomaly at day 10 minus that at day 5. This figure clearly illustrates the importance of Kelvin wave dynamics in the solution.

about 55 cm sec^{-1}) of the region of reduced upwelling near
the western end of the zonal segment. This occurs whether
the model is started from rest or from the quasi-balanced
initial state. However, the weak waves which trail the
main front when the model is driven from rest are absent
when it is driven from the quasi-balanced state. Fig. 17c
clearly shows a weak spurious Kelvin wave near y = - 300 km
excited by the southern boundary conditions at f = 4×10^{-5}
sec^{-1}. Southern boundaries at higher latitudes would gene-
rate weaker Kelvin waves.

The wind was shut off at day 5, thus removing the con-
straint positioning the enhanced upwelling at the eastern
end of the zonal segment and the reduced upwelling at the
western end. Fig. 15c,d and Fig. 17c,d show that these
regions have propagated along the coast. This has actually
lead to significant upwelling at the western end of the
zonal section of coastline after the wind was shut off
(Figs. 15d and 17d). Fig. 18 shows that the baroclinic
mode tends to separate from the coast after the wind has
been shut off.

Fig. 19a shows the pycnocline height anomaly at day 5
for Case b. The pattern can be explained in a manner simi-
lar to that for Case a, but this time the enhanced upwelling
occurs at the western end of the zonal segment and reduced
upwelling occurs at the eastern end. The 7 m difference in
occurs at the western end of the zonal segment and reduced
upwelling occurs at the eastern end. The 7 m difference in
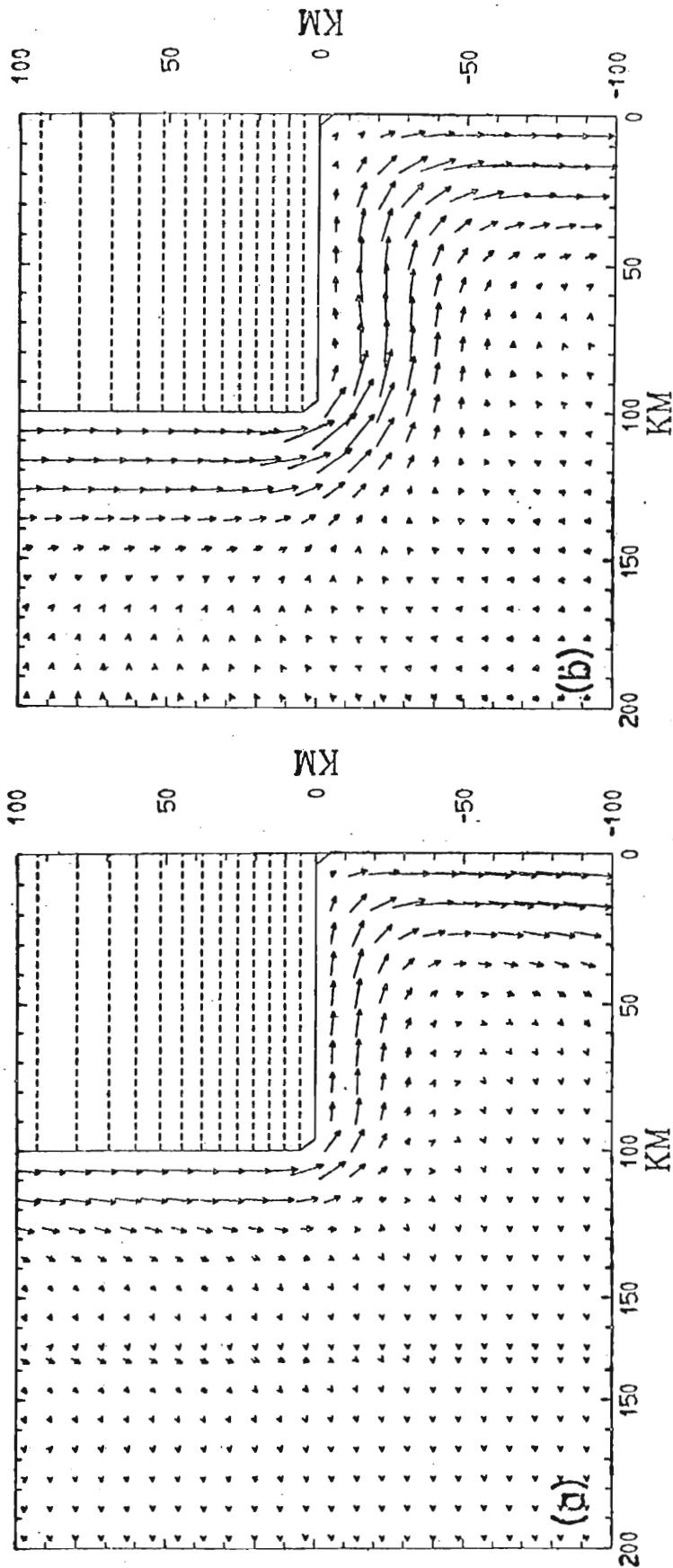the height anomaly between Cases a and b at the center of

Fig. 18. $\vec{V}_1 - \vec{V}_2$ at day 5 (a) and day 10 (b) for Case a. The wind was shut off at day 5. Note that by day 10 the current has broadened and along the zonal segment has separated from the coast.
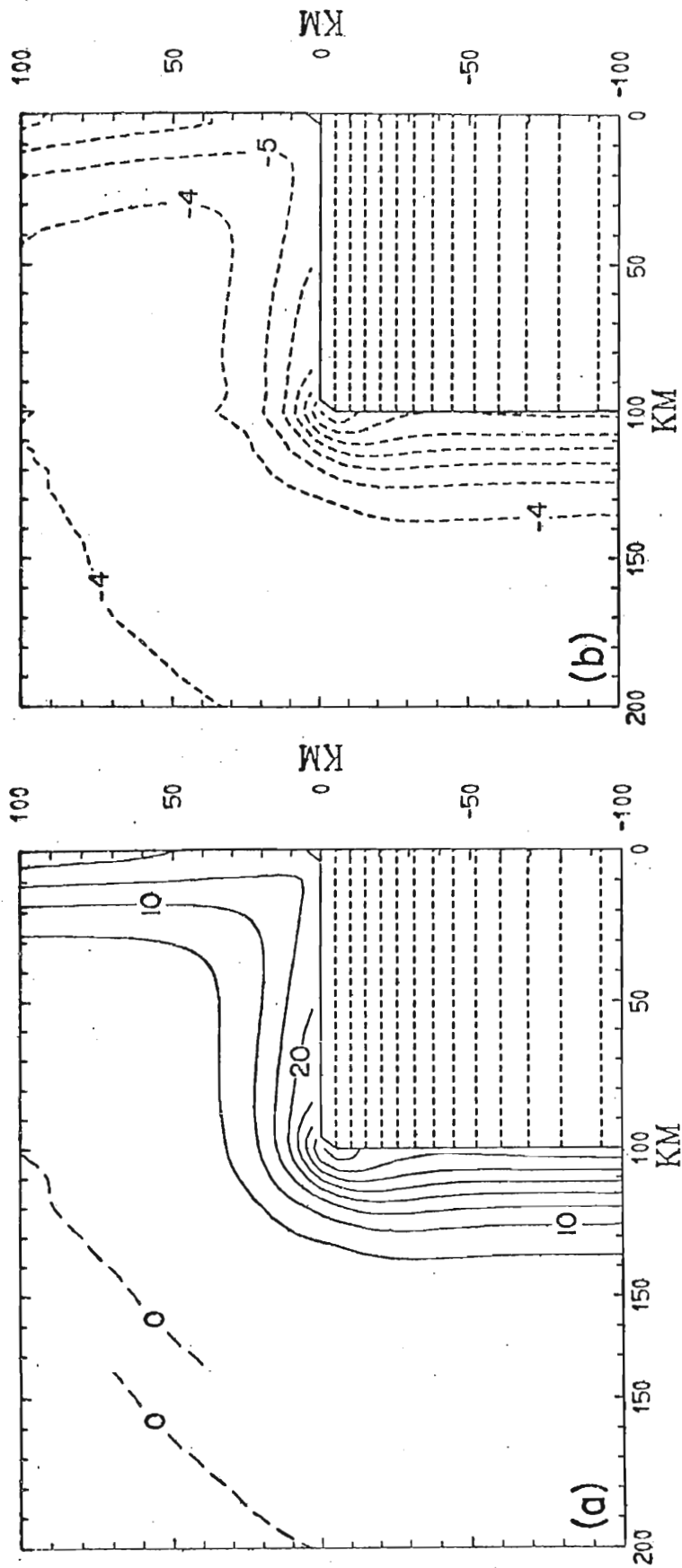
Fig. 19. Pycnocline height anomaly in m (a) and free
surface anomaly in cm (b) for Case b at day 5.

the zonal segment reflects the direct (3.5 m) effect of the
wind stress normal to the coast. In the case of a cape and
an equatorward wind stress this would lead to only slightly
enhanced upwelling on the south side of the cape and must
not be considered a significant factor. The propagating
Kelvin waves produce greater effects.

The pattern of the free surface anomaly for Case b at
day 5 (Fig. 19b) is almost the same as for the pycnocline
anomaly, indicating the overwhelming dominance of the baro-
clinic mode in the solution. Fig. 20a,b shows the barotropic
mode for Cases a and b. The most notable features are the
cyclonic eddies adjacent to the zonal segments. Note also
the double current structure parallel to the meridional
segments and the westward currents which extend beyond the
zonal coastline. The maximum velocity associated with the
barotropic mode in Fig. 20 is 3 cm sec^{-1}. Recall Hurlburt
and Thompson (1973) have shown that for the case with a
Sverdrup interior, a meridional coastline, flat topography,
and no wind stress curl in the upwelling zone, the net long-
shore transport must nearly vanish point by point across the
upwelling zone. They also explain the nonlinear dynamics of
the weak barotropic equatorward current observed about 25 km
off shore in Fig. 20. Bottom friction and nonlinearities,
especially the nonlinearity due to the denominator of the
wind stress forcing function, are responsible for the baro-
especially the nonlinearity due to the denominator of the
wind stress forcing function, are responsible for the baro-
tropic mode in the case just described.
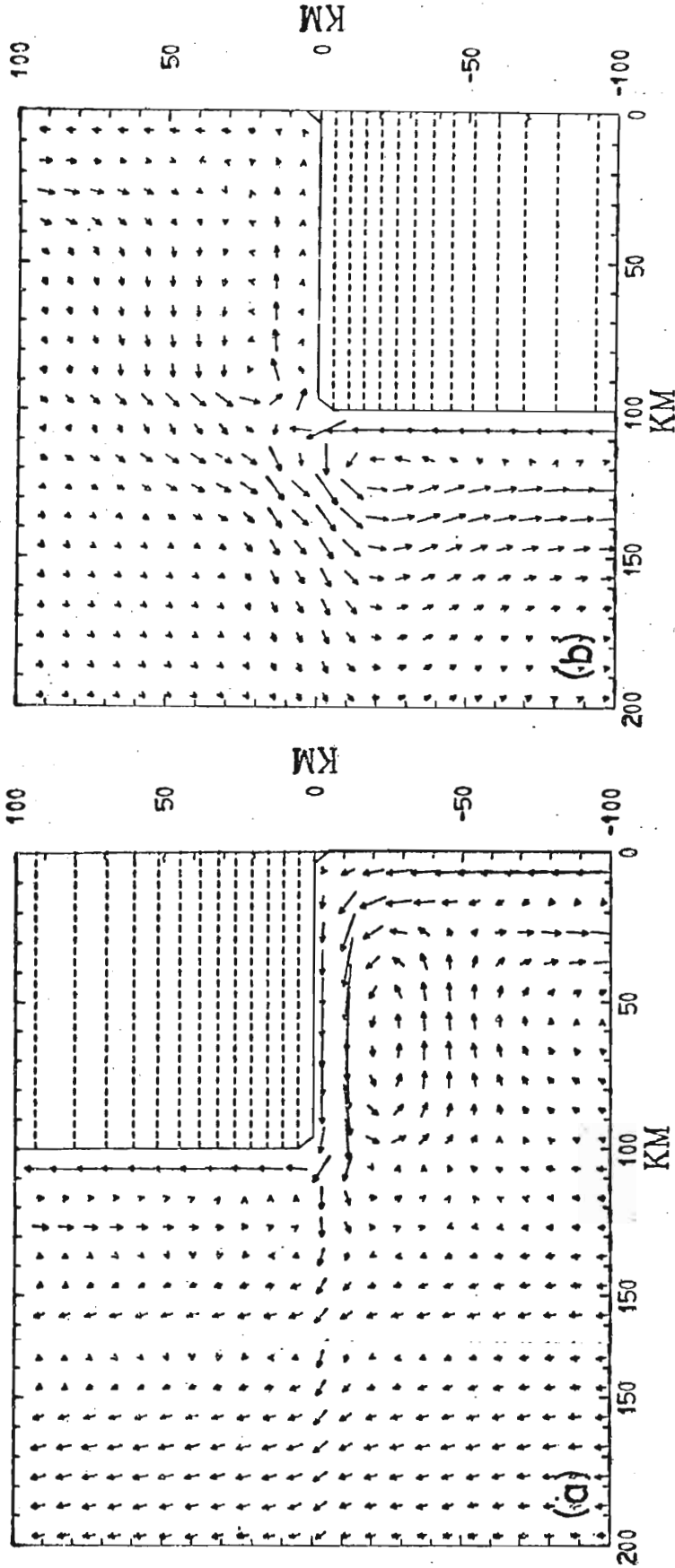
Fig. 20. Barotropic transports for Case a (a) and
Case b (b) at day 5.

Fig. 21 shows contours of potential vorticity in the lower layer at days 5 and 10 for Case a and day 5 for Case b. Since conservation of potential vorticity is a good approximation for these solutions outside the viscous boundary layers, Fig. 21 and slow time variation of the contours of potential vorticity show that the fluid particles in the upwelling boundary layer should follow the coastline and remain in the boundary layer for great distances, O(1000 km), along the coast, a point with important implications for biologists and environmentalists. However, recall from (35) that potential vorticity may not be well conserved in the presence of wind stress curl or sloping topography. The wave-like feature on the 325 contour in Fig. 21c is consistent with the pattern of relative vorticity for the barotropic mode (Fig. 20b). Note the -4 cm contour of the free surface anomaly (Fig. 19b) also shows a slight spike in this region. A similar but much weaker feature (not shown in Fig. 21a,b) occurs in Case a south of the western end of the zonal section.

b.   Effects of mesoscale
     capes and bays

The effects of coastline geometry are further illustrated by Cases c through f. Fig. 22a,b depicts the solution at day 5 for a rectangular cape, 51×30.7 km. Fig. 22a demonstrates that, as before, the longshore currents follow the coastline with only a slight tendency to separate from demonstrates that, as before, the longshore currents follow the coastline with only a slight tendency to separate from the zonal segments. The coastal current is oppositely

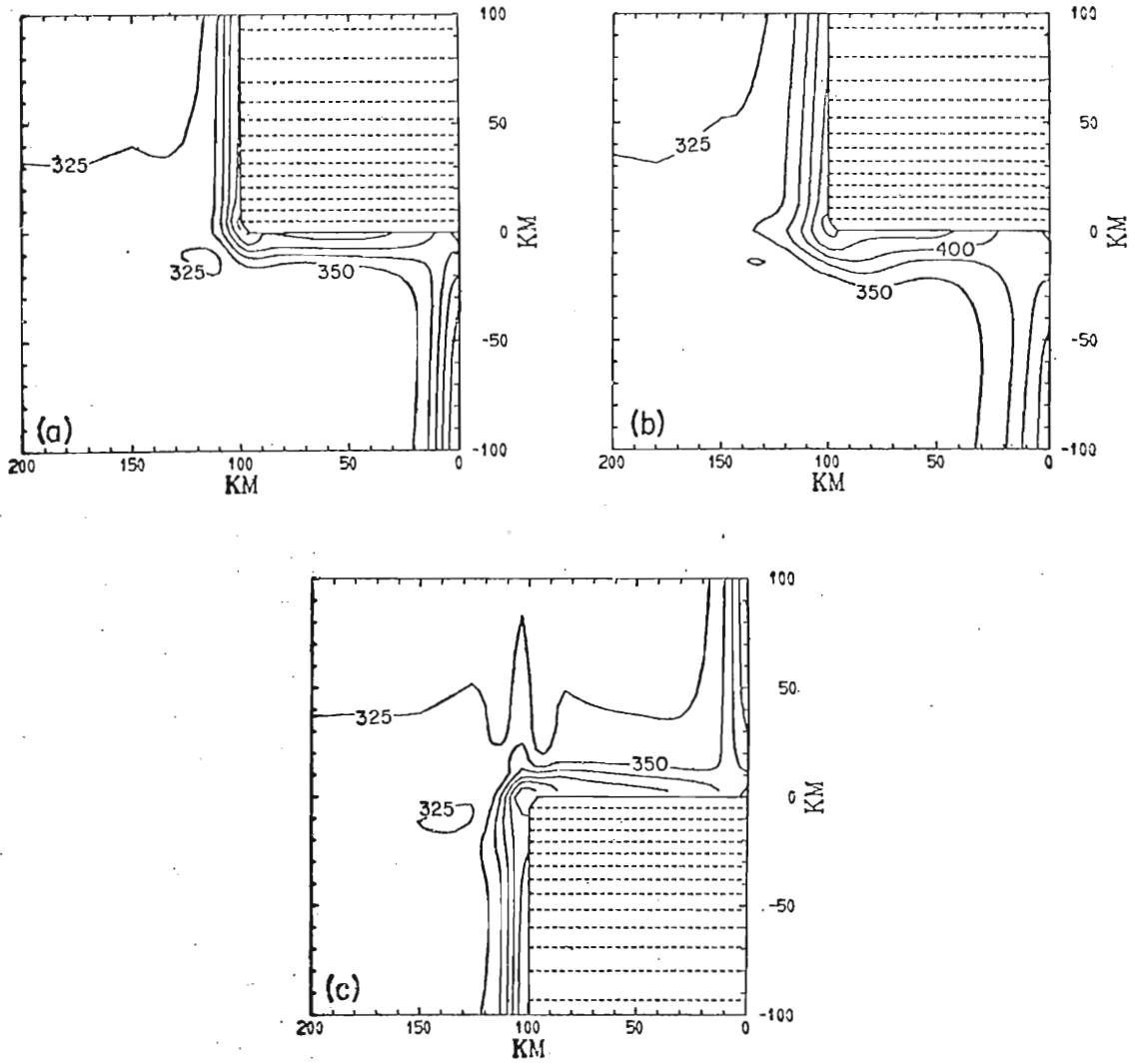Fig. 21. Lower layer potential vorticity in cm^{-1} $sec^{-1} \times 10^{-7}$ for Case a at days 5 (a) and 10 (b) and for Case b at day 5 (c). The wind was shut off at day 5.
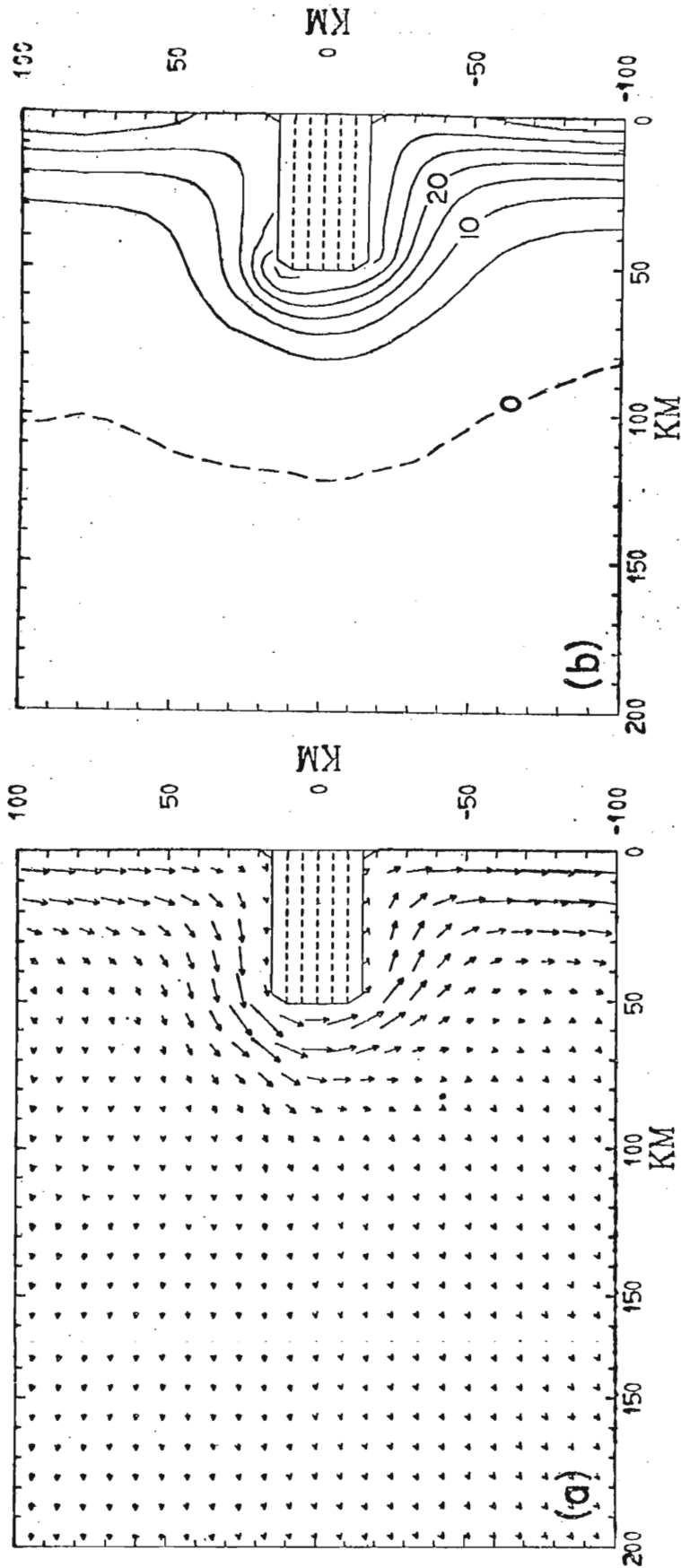
Fig. 22. Upper layer velocity (a) and pycnocline
height anomaly in m (b) for Case c at day 5.

directed in the lower layer. The pycnocline height anomaly
(Fig. 22b) shows a pattern which is a combination of the
effects found in Cases a and b. Strong upwelling occurs
along all parts of the zonal segments of the coastline, but
is weaker at the eastern end of the northern segment and
stronger at the western end. Oppositely along the southern
segment, it is weaker near the western end and stronger near
the eastern end. The upwelling at the center of the southern
segment is slightly stronger than at the center of the north-
ern segment. The weaker upwelling along the northern meri-
dional segment reflects the northward propagation of the
weaker upwelling near the eastern end of the northern zonal
segment (cf. Fig. 17).

Fig. 23 illustrates the solution at day 5 near a cape
resembling the coastline in the vicinity of Point Concepcion,
California. Fig. 23a shows again that the equatorward sur-
face jet follows the coast. The weak current overshooting
the end of the cape indicates the presence of a weak cyclonic
eddy in the barotropic mode off the point of the cape. The
coastal current is oppositely directed in the lower layer.
Fig. 23b shows that the upwelling follows the coastline, but
otherwise this cape exhibits no dramatic effect on the pat-
tern of vertical motion. Upwelling is greatest near the
point of the cape and slightly greater on the southern side
then on the northern side. The strength of the upwelling
point of the cape and slightly greater on the southern side
then on the northern side. The strength of the upwelling
varies by about 35 per cent along the cape.
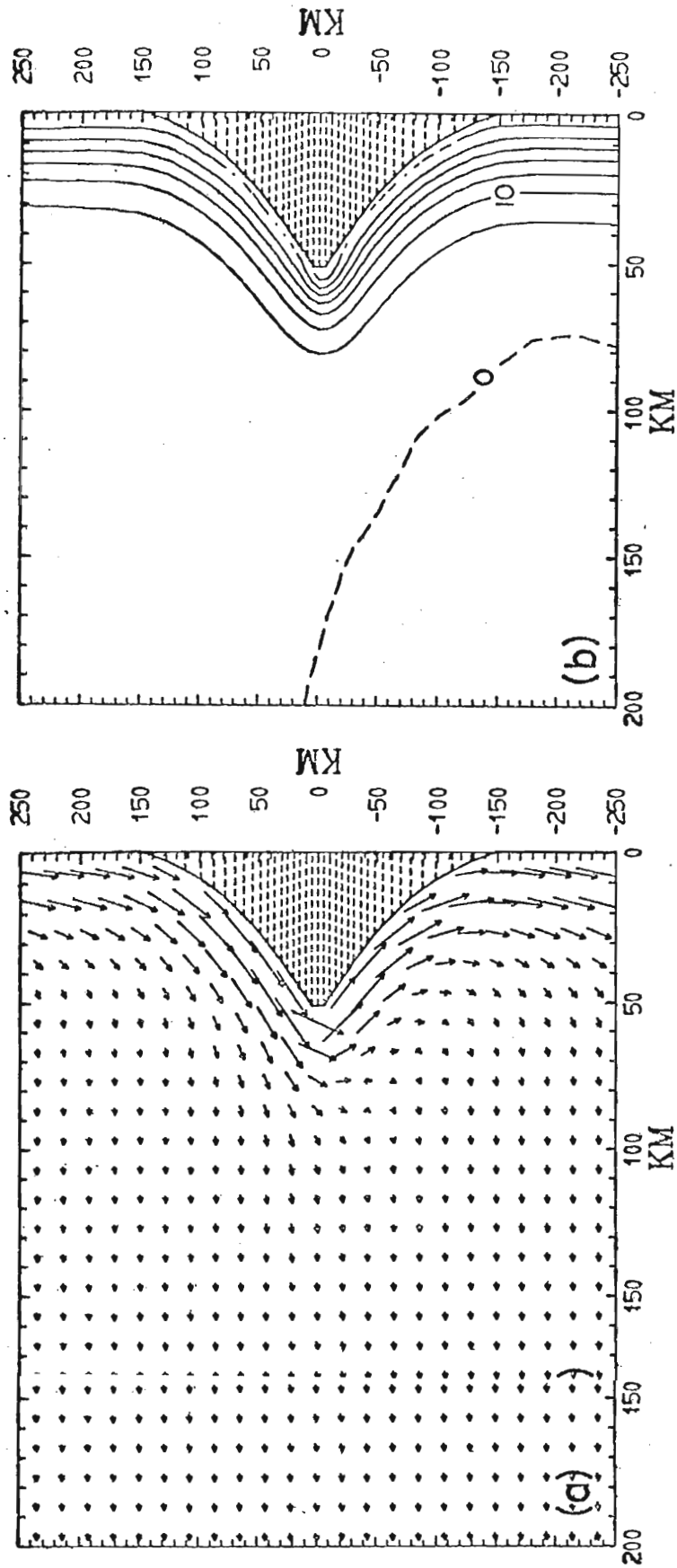
Fig. 23. Upper layer velocity (a) and pycnocline height anomaly in m (b) for Case d at day 5.

Fig. 24 depicts the solution in the vicinity of a bay at day 5. As before, the equatorward surface jet (Fig. 24a) and the poleward undercurrent follow the coastline. The pattern of vertical motion also follows the coast. The upwelling at the coast exhibits a distinct minimum at the center of the bay, nearly 20 per cent less than along the meridional segments. The E-W amplitude of the 5 m contour is 42 km compared to the 51 km amplitude of the bay.

The final case to be discussed (Case f) is the only one to incorporate both coastline variations and sloping topography (see Fig. 14). Thus, it is also the only case with coastline variations to be discussed which has a significant barotropic mode. The same bay geometry as Case e is employed. The bottom topography follows the coastline with a uniform E-W slope of 2×10^{-3}, the same basic slope used in Section 4. The initial upper layer thickness (30 m), and the height of the topography above the reference level at the coast (155 m) are also the same. Fig. 25a,b shows the upper and lower layer velocities at day 5. As in Cases a through e, the coastal currents follow the coastline and as in the cases with similar basic topography discussed in Section 4 there is no poleward undercurrent along the meridional sections of the coastline. However, there is a weak and narrow poleward undercurrent along almost all of the non-meridional coastline, which barely shows up in Fig. 25b. and narrow poleward undercurrent along almost all of the non-meridional coastline, which barely shows up in Fig. 25b. The width of the current is < 10 km and the maximum velocity
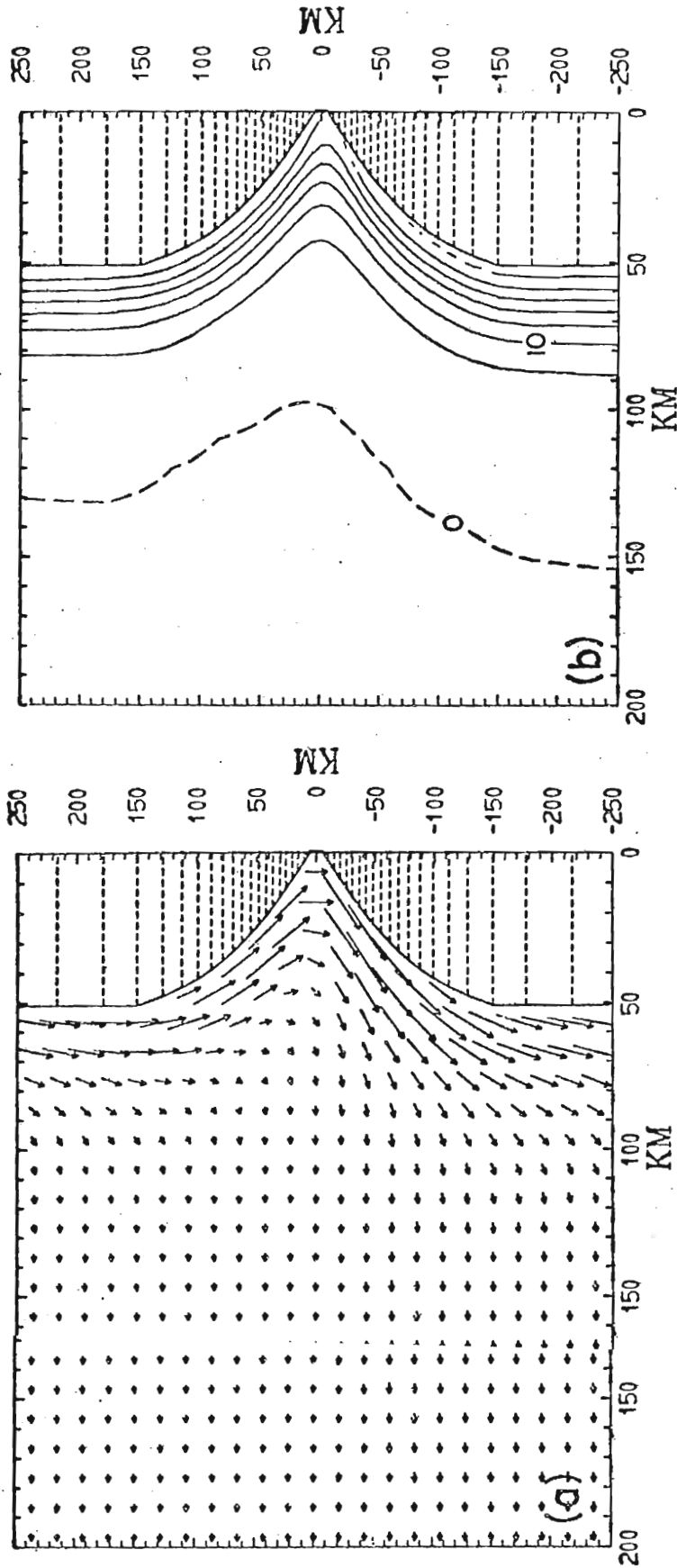
Fig. 24. Upper layer velocity (a) and pycnocline height
anomaly in m (b) for Case e at day 5.
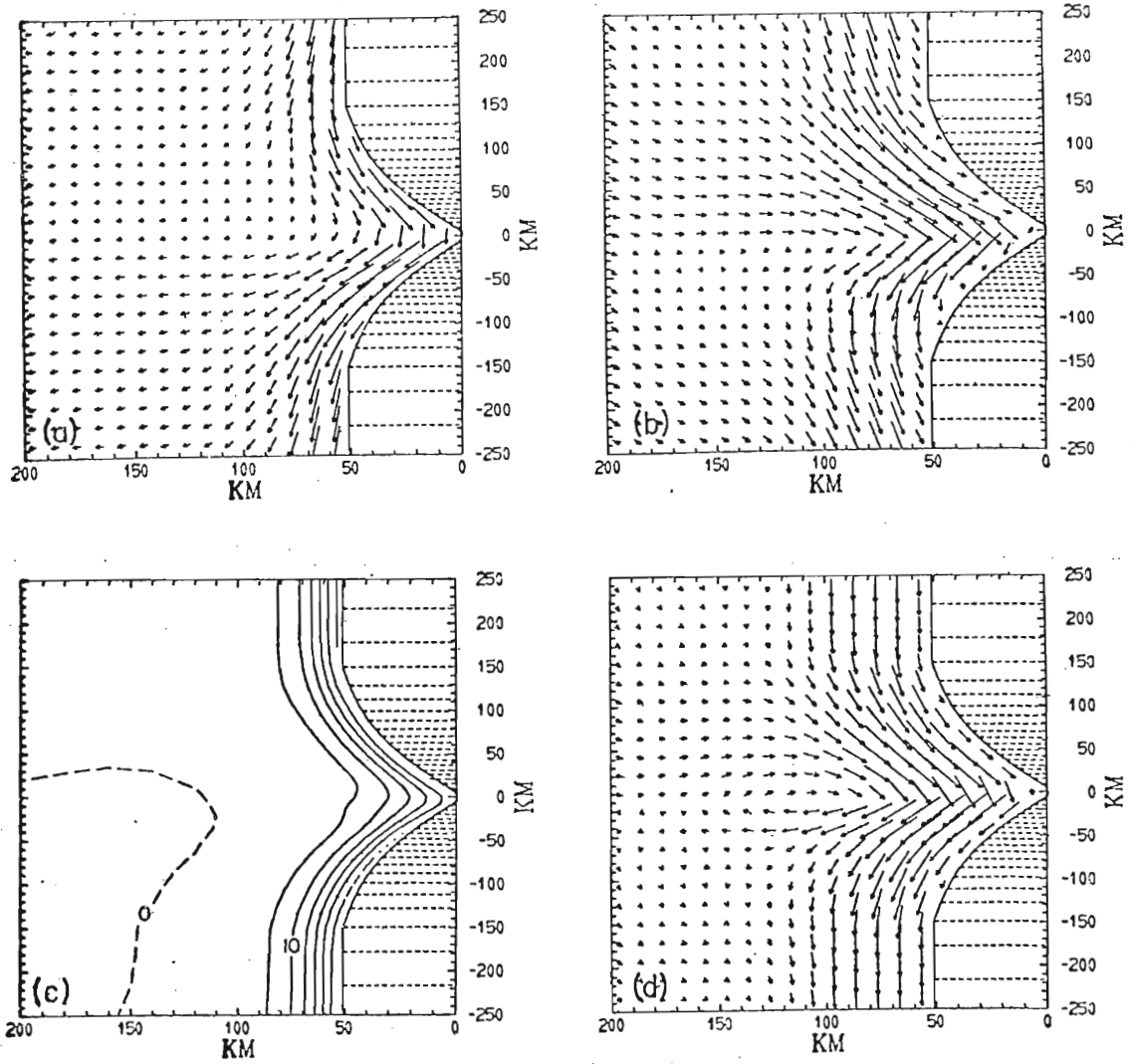
Fig. 25. Upper layer velocity (a), lower layer velocity (b), pycnocline height anomaly in m (c) and the barotropic transport (d) for Case f at day 5.

is about 3 cm sec^{-1}. The maximum width and strength of the current occurs at y = 0. Fig. 25c shows that the upwelling follows the coast. As in Case e the upwelling at the coast exhibits a distinct minimum near y = 0.

Fig. 25d shows the barotropic mode at day 5. The maximum speed is about 15 cm sec^{-1}. The velocities associated with the eddy are approximately 1 cm sec^{-1}, about the same as the general onshore return flow in the lower layer as demonstrated by Fig. 25b. It is also similar in strength to the barotropic flows which occurred in the flat bottom case due to nonlinear effects and bottom stress.

6. SUMMARY AND CONCLUSIONS

In the present study an x-y-t two-layer, primitive equation model on a β-plane has been used to investigate three-dimensional aspects of the wind-driven eastern ocean circulation, emphasizing the effects of various configurations of bottom topography and coastline geometry on coastal currents and the pattern of vertical motion. The model is time-dependent and retains the free surface. It is integrated using an efficient semi-implicit numerical scheme and a variable resolution grid which allows resolution of mesoscale boundary layers and longshore features, and a model region with an E-W extent great enough to permit development of a Sverdrup interior. A unique feature of the model is a quasi-symmetric open-basin northern and southern boundary condition which allows development of a Sverdrup interior even when the model is solved on regions with mesoscale N-S extent.

Several case studies which demonstrate the role of the northern and southern boundary conditions have been compared in Section 3. They show that solutions for a closed basin on a β-plane, an open basin on a β-plane using quasi-symmetric northern and southern boundary conditions, and basin on a β-plane, an open basin on a β-plane using quasi-symmetric northern and southern boundary conditions, and the quasi-symmetric x-z plane model of Hurlburt and Thompson (1973) are in close agreement. The influence on the

barotropic mode of coastline orientation, wind stress distribution, wind stress curl in the upwelling zone, and bottom topography have also been discussed in Section 3. In particular, β-plane solutions with longshore winds were found insensitive to the coastline orientation for large departures from the meridional. The manner in which the distribution of the wind stress may affect the N-S pressure gradient in an f-plane solution is also demonstrated.

In Section 4 the effects of longshore variations in topography were discussed. The topographic β effect was found to be an important aspect of the dynamics even for mesoscale features, $O(100$ km$)$. For an equatorward wind stress, $\beta_T > 0$ (cf. Eq. (33)) contributes a poleward component to the flow, $\beta_T < 0$ an equatorward component. Due to the E-W slope in the topography potential vorticity is not conserved. The streamlines make only distorted attempts to follow the isobaths. The longshore variations in topography also produce barotropic flows well beyond their physical extent, both longshore and offshore, in response to requirements of mass continuity. These flows appear to respond on a scale governed by the barotropic radius of deformation. Quite striking in all the solutions with longshore variations in topography is the lack of noticeable wave phenomena associated with the topographic perturbations,

shore variations in topography is one lack of noticeable wave phenomena associated with the topographic perturbations, except for the northward propagation of one barotropic feature after the wind is shut off.

Section 5 discussed the effects of mesoscale, 0(100 km), coastline variations. The salient results will be summarized in terms of a 51×30.7 km rectangular cape (cf. Fig. 22). The coastal currents and the upwelling were found to follow the coastline. Thus, strong upwelling not driven directly by the wind occurs along the zonal segments of the coastline. However, it is weaker at the eastern end of the northern segment and stronger at the western end. Oppositely, it is weaker near the western end of the southern segment and stronger near the eastern end. This demonstrates that the continuity of the baroclinic coastal jet is partitioned between a vertical circulation and a circulation in the horizontal plane. (See Section 5a for a more detailed discussion.) The upwelling at the center of the southern E-W segment of the cape is only slightly stronger than at the center of the northern segment due to the direct effect of winds normal to the coast.

When the wind is turned off the distribution of upwelling is no longer constrained to the coastal positions described, but instead, propagates along the coast near the speed of an internal Kelvin wave. Thus, significant upwelling can occur at some regions along the coast even after the winds have been shut off. The region of weak upwelling at the eastern end of the northern E-W segment propagates northward as a large amplitude Kelvin wave while the wind at the eastern end of the northern E-W segment propagates northward as a large amplitude Kelvin wave while the wind stress is still acting. Thus, regions north of the cape may

experience depressed upwelling and temporary downward verti-
cal motion under equatorward wind stress forcing. The work
of Suginohara (1973) and Gill and Clarke (1973) on the
effects of the wind stress distribution, and the present
work on the effects of coastline geometry have identified
Kelvin wave dynamics as an element of fundamental importance
to the coastal upwelling problem.

APPENDICES

APPENDIX A

LIST OF SYMBOLS

A	horizontal eddy viscosity
C_I, C_B	drag coefficients for interfacial and bottom friction
D	height of the bottom topography above a reference level
f	Coriolis parameter
g	acceleration due to gravity
g'	reduced gravity, $g(\rho_2 - \rho_1)/\rho_2$
h	total depth
h_1, h_2	instantaneous local thickness of the layers
H_1, H_2	initial thickness of the layers
L_v	width of the viscous boundary layer in the y-momentum equation
L_x, L_y	total extent of the model region in the x and y directions
N	Brunt-Väisälä frequency
t	time
u, v	barotropic components of velocity in the x and y directions
u_1, u_2	x-directed components of current velocity
v_1, v_2	y-directed components of current velocity
x, y, z	tangent plane Cartesian coordinates: x positive eastward, y positive northward, z positive upward

93

β	df/dy
β_T	value of β simulated by N-S sloping topography
Δt	time increment in the numerical integration
$\Delta x, \Delta y$	horizontal grid increments in the x and y directions
ζ	free surface anomaly
λ	baroclinic radius of deformation
λ_E	barotropic radius of deformation
ρ, ρ_1, ρ_2	densities of sea water
$\tau_{sx}, \tau_{Ix}, \tau_{Bx}$	x-directed tangential stresses at the surface, interface, and bottom
$\tau_{sy}, \tau_{Iy}, \tau_{By}$	y-directed tangential stresses at the surface, interface, and bottom

APPENDIX B

AN OPEN-BASIN BOUNDARY CONDITION FOR OCEAN MODELS

Consider a stably-stratified rotating ocean model on a β-plane with solid eastern and western boundaries, but open-basin northern and southern boundaries. We will discuss a northern and southern boundary condition which permits development of a Sverdrup interior even when the portion of the basin solved has only a mesoscale N-S extent. However, the E-W scale, 0(1000 km) or more, cannot be relaxed if the model is to develop a Sverdrup interior without the imposition of some additional constraint.

Our discussion will be in terms of a two-layer, vertically-integrated primitive equation model which is hydrostatic and Boussinesq and which neglects thermodynamics and thermohaline mixing. A similar condition could be developed for other model formulations. Under the assumptions given, the momentum equations and equations of continuity form the following closed set for an x-y-t two-layer model on a β-plane:

$$\frac{\partial \vec{V}_1}{\partial t} + \vec{V}_1 \cdot \nabla \vec{V}_1 + \hat{k} \times f\vec{V}_1 = -g\nabla(h_1+h_2+D) + \frac{\vec{\tau}_s - \vec{\tau}_I}{\rho h_1} + A\nabla^2 \vec{V}_1$$

(1)

$$\frac{\partial h_1}{\partial t} + \nabla \cdot (h_1 \vec{V}_1) = 0 \tag{2}$$

(1)

$$\frac{\partial h_1}{\partial t} + \nabla \cdot (h_1 \vec{V}_1) = 0 \tag{2}$$

95

$$\frac{\partial \vec{V}_2}{\partial t} + \vec{V}_2 \cdot \nabla \vec{V}_2 + \hat{k} \times f\vec{V}_2 = - g\nabla(h_1+h_2+D) + g'\nabla h_1 +$$

$$\frac{\vec{\tau}_I - \vec{\tau}_B}{\rho h_2} + A\nabla^2 \vec{V}_2 \qquad\qquad (3)$$

$$\frac{\partial h_2}{\partial t} + \nabla \cdot (h_2 \vec{V}_2) = 0 \qquad\qquad (4)$$

where 1 denotes the upper layer, 2 the lower layer,

$$\nabla = \frac{\partial}{\partial x} \hat{i} + \frac{\partial}{\partial y} \hat{j}$$

$$\vec{V}_1 = u_1 \hat{i} + v_1 \hat{j}$$

$$f = f_0 + \beta(y - y_0)$$

$$g' = g(\rho_2 - \rho_1)/\rho_2$$

$$\vec{\tau}_s = \tau_{sx}\hat{i} + \tau_{sy}\hat{j}$$

$$\vec{\tau}_I = \rho C_I |\vec{V}_1 - \vec{V}_2|(\vec{V}_1 - \vec{V}_2)$$

$$\vec{\tau}_B = \rho C_B |\vec{V}_2| \vec{V}_2$$

and $i = 1, 2$. Symbols are defined in Appendix A, although most of the notation used is common in oceanography. $D(x)$ represents the height of the bottom topography above a re-ference level. The formulation of the interfacial and bottom stresses follows O'Brien and Hurlburt (1972), but has been modified slightly to be invariant under coordinate transformation.

The northern and southern boundary conditions are transformation.

The northern and southern boundary conditions are based on the x-z plane model of Hurlburt and Thompson (1973)

which neglects longshore derivatives of the velocity field
and the wind stress, but retains the N-S pressure gradient
and the β effect. Hurlburt and Thompson discuss in detail
the derivation of their model, which we will refer to as
quasi-symmetric because of its partial neglect of longshore
derivatives. Two crucial requirements for this boundary
condition to be applicable are that the longshore flow be
nearly geostrophic and that

$$\left| \int_{-L_x}^{X} f \, \frac{v_i}{y} \, dx \right| \ll \left| \int_{-L_x}^{X} \beta v_i \, dx \right|$$

near the northern and southern boundaries, where $-L_x$ is at
the western boundary. Since $f \, (\partial v_1 / \partial y)$ may be comparable
to βv_i in the eastern boundary layers, the latter require-
ment essentially demands that the N-S pressure gradient
exhibit only a second order change across these eastern
layers. The longshore flow may be nearly geostrophic even
into the hydrostatic viscous boundary layer. Geostrophy
holds in this layer because the velocity component aspect
ratio, u_i / v_i, is $0(10^{-1})$.

In summary, the quasi-symmetric boundary condition
sets $\partial / \partial y = 0$ in (1) through (4) except for the N-S pressure
gradient in the momentum equations and $\partial h v_i / \partial y$ in the conti-
nuity equations. The N-S pressure gradients are given by

$$g \, \frac{\partial}{\partial y} \, (h_1 + h_2 + D) = \int^{X} \beta \, (v_1 - v_A) \, dx + g \, \frac{\partial}{\partial y} \, (h_1 + h_2 + D) \Big|_{-L_x} \quad (6)$$

$$g \, \frac{\partial}{\partial y} \, (h_1 + h_2 + D) = \int_{-L_x}^{X} \beta \, (v_1 - v_A) \, dx + g \, \frac{\partial}{\partial y} \, (h_1 + h_2 + D) \Big|_{-L_x} \quad (6)$$

$$g \frac{\partial}{\partial y} (h_1+h_2+D) - g' \frac{\partial h_1}{\partial y} = \int_{-L_x}^{x} \beta \left[v_2 + \frac{h_1}{h_2} v_A\right] dx$$

$$+ g \frac{\partial}{\partial y} (h_1+h_2+D)\bigg|_{-L} - g' \frac{\partial h_1}{\partial y}\bigg|_{-L_x} \tag{7}$$

where

$$v_A = v_1 - \left[v_1 h_1 + \left(v_2 + \frac{g'}{f} \frac{\partial h_1}{\partial x}\right) h_2\right]\bigg/(h_1+h_2) \tag{8}$$

Note that application of the Hurlburt and Thompson model as a boundary condition has required two significant modifications. First, the term $\partial h_i v/\partial y$ is retained in the continuity equations. The second difference is the manner in which the ageostrophic part of the departure from a modified depth average of v given by (8) is removed in (6) and (7). Hurlburt and Thompson show that the N-S pressure gradient which develops due to the vorticity constraint of a Sverdrup interior responds primarily to the geostrophic N-S flow. Note that neither the barotropic nor the baroclinic component of the geostrophic flow is affected by v_A. The most significant ageostrophic components of the N-S flow are inertial oscillations and Ekman drift, both of which are effectively removed from (6) and (7) by (8). Were these not removed, (6) and (7) show they would result in spurious contributions to the N-S pressure gradient at the northern and southern boundaries. This effect would propagate into the interior as gravity waves which are observed in numeri-
and southern boundaries. This effect would propagate into the interior as gravity waves which are observed in numerical solutions when we set $v_A = 0$. Since the N-S pressure

gradient may affect the strength of the circulation in the plane normal to the coast, inertial oscillations in this pressure gradient could also excite Kelvin waves. Again these have been found in numerical solutions when we set $v_A = 0$.

Several other techniques for the removal of ageostrophic components from v in (6) and (7) have been investigated, but the use of (8) is the only one which has not led to instabilities such as amplification of the fundamental barotropic E-W mode of the basin.

The value of the N-S pressure gradient at the western boundary should be determined by an integral constraint on the mass flux through the boundary, but for some applications it may be sufficient to arbitrarily set it to zero. This has been done in both applications considered by the author thus far.

The northern and southern boundary conditions described here have been tested on two quite different problems. The first is a study of the eastern ocean circulation driven by an equatorward wind stress. Several different cases which demonstrate the role of the northern and southern boundary conditions are compared in Section. 3. It is important to note that solutions for a closed basin on a β-plane, the quasi-symmetric boundary conditions described here, and the x-z plane model of Hurlburt and Thompson are essentially the quasi-symmetric boundary conditions described here, and the x-z plane model of Hurlburt and Thompson are essentially the same in the interior and the eastern ocean. They may be different in the western ocean, if the N-S pressure gradients

at the western boundary of the quasi-symmetric condition are not determined by an integral constraint on the total mass flux through the northern and southern boundaries.

The second study was a simulation of the narrow seasonal equatorial jet driven by a west wind in the Indian Ocean (results to be discussed elsewhere). In this case open basin boundary conditions which set $\partial v_i / \partial y = 0$ in the continuity equation or alternatively set $\partial h_i / \partial y = 0$ in the y-momentum equation produce amplification of the fundamental barotropic E-W mode of the basin which renders the solutions useless after 3 or 4 days of model time, but the one described here has yielded excellent results for a 75 day integration.

REFERENCES

Allen, J. S., 1973: Upwelling and coastal jets in a conti-
    nuously stratified ocean. J. Phys. Oceanogr., 3,
    245-257.

Arthur, R. S., 1965: On the calculation of vertical motion
    in the eastern boundary currents from determinations
    of horizontal motion. J. Geophys. Res., 70, 2799-
    2803.

Charney, J. G., 1955: The generation of oceanic currents
    by wind. J. Marine Res., 14, 477-498.

Crank, J., and P. Nicholson, 1947: A practical method for
    numerical evaluation of solutions of partial dif-
    ferential equations of heat-conduction type. Proc.
    Camb. Philos. Soc., 43, 50-67.

Ekman, V. W., 1905: On the influence of the earth's rota-
    tion on ocean currents. Arkiv. Mat. Astron. Fysik,
    12, 1-52.

Garvine, R. W., 1971: A simple model of coastal upwelling
    dynamics. J. Phys. Oceanogr., 1, 169-179.

Gill, A. E., and A. J. Clarke, 1973: Wind-induced upwelling,
    coastal currents and sea-level changes. (Unpublished
    manuscript)

Grammeltvedt, A., 1969: A survey of finite-difference
    schemes for the primitive equations for a barotropic

Grammeltvedt, A., 1969: A survey of finite-difference
    schemes for the primitive equations for a barotropic
    fluid. Mon. Wea. Rev., 97, 384-404.

Hidaka, K., 1954: A contribution to the theory of upwelling and coastal currents. Trans. Amer. Geoph. Union, 35, 431-444.

Hurlburt, H. E., and J. D. Thompson, 1973: Coastal upwelling on a β-plane. J. Phys. Oceanogr., 3, 16-32.

Kindle, J. C., and J. J. O'Brien, 1974: On upwelling along a zonally-oriented coastline. (To appear in J. Phys. Oceanogr., 4(1).)

Kwizak, M., and A. Robert, 1971: A semi-implicit scheme for grid point atmospheric models of the primitive equations. Mon. Wea. Rev., 94, 32-36.

McNider, R. T., and J. J. O'Brien, 1973: A multi-layer transient model of coastal upwelling. J. Phys. Oceanogr., 3, 258-273.

Mooers, C. N. K., C. A. Collins, and R. L. Smith, 1972: The dynamic structure of the frontal zone in the coastal upwelling region off Oregon. (Submitted to J. Phys. Oceanogr.)

O'Brien, J. J., 1973: Analytical solutions for two-layer models of the onset of a coastal upwelling event. (Submitted to J. Phys. Oceanogr.)

O'Brien, J. J., and H. E. Hurlburt, 1972: A numerical model of coastal upwelling. J. Phys. Oceanogr., 2, 14-26.

Pedlosky, J., 1974: On coastal jets and upwelling in bounded basins. (To appear in J. Phys. Oceanogr., 4(1).)

bounded basins. (To appear in J. Phys. Oceanogr., 4(1).)

Proudman, J., 1953: Dynamical Oceanography. London, Methuen, 409 pp.

Sarkisyan, A. S., 1969: Deficiencies of barotropic models of oceanic circulation. Izv., Atmospheric and Oceanic Physics, 5, 818-835. (English trans., 446-474)

Sarkisyan, A. S., and V. F. Ivanov, 1971: Joint effect of baroclinicity and bottom relief as an important factor in the dynamics of sea currents. Izv., Atmospheric and Oceanic Physics, 7, 173-188. (English trans., 116-124)

Schulman, E. E., 1970: The antarctic circumapolar current Proc. of the 1970 Summer Computer Simulation Conference, Denver, Colorado, 955-968.

Stevenson, M. R., R. W. Garvine, and B. Wyatt, 1973: Lagrangian measurements in a coastal upwelling zone off Oregon. (Submitted to J. Phys. Oceanogr.)

Suginohara, N., 1973: Coastal upwelling in a two-layer ocean by wind stress with longshore variation. (Unpublished manuscript)

Thompson, J. D., 1974: The coastal upwelling cycle on a beta-plane: hydrodynamics and thermodynamics. Ph.D. Thesis, Florida State University (in preparation).

Thompson, J. D., and J. J. O'Brien, 1973: Time-dependent coastal upwelling. J. Phys. Oceanogr., 3, 33-46.

Yoshida, K., 1955: Coastal upwelling off the California Coast. Rec. Ocn. Works in Japan, 2, 8-20.

Yoshida, K., 1967: Circulation in the eastern tropical oceans with special reference to upwelling and undercurrents. Japan J. Geophys., 4, 1-75.

oceans with special reference to upwelling and under-currents. Japan J. Geophys., 4, 1-75.

Yoshida, K., 1973: The coastal undercurrent — the baroclinicity of the coastal upwelling processes. (Unpublished manuscript presented at the CUEA Theoretical Workshop at Oregon State University, August, 1973)

VITA

Harley E. Hurlburt was born on April 12, 1943 in Bennington, Vermont. He graduated from Bennington High School in 1961 and received a B.S. in Physics from Union College, Schenectady, N.Y. in 1965. He then spent four years as a Weather Officer in the USAF with assignments at The Pennsylvania State University, Andersen AFB, Guam, and the Development Branch of the Air Force Global Weather Central, Offutt AFB, Nebraska. He received an M.S. in Meteorology from The Florida State University in 1971.